The Astrophysical Journal, 916:73 (23pp), 2021 August 1 https://doi.org/10.3847/1538-4357/ac05c2

A Comparison between Nuclear Ring Star Formation in LIRGs and in Normal Galaxies with the Very Large Array

Y. Song[1], S. T. Linden[2], A. S. Evans[1,3], L. Barcos-Muñoz[3], G. C. Privon[3], I. Yoon[3], E. J. Murphy[3], K. L. Larson[4], T. Díaz-Santos[5,6,7], L. Armus[4], Joseph M. Mazzarella[4], J. Howell[4], H. Inami[8], N. Torres-Albà[9], V. U[10], V. Charmandaris[7,11], J. McKinney[2], D. Kunneriath[3], and E. Momjian[12]
[1] Department of Astronomy, University of Virginia, 530 McCormick Road., Charlottesville, VA 22904, USA; ys7jf@virginia.edu
[2] Department of Astronomy, University of Massachusetts, LGRT-B 618, 710 North Pleasant Street, Amherst, MA 01003, USA
[3] National Radio Astronomy Observatory, 520 Edgemont Road, Charlottesville, VA 22903, USA
[4] IPAC, Mail Code 314-6, Caltech, 1200 E. California Boulevard, Pasadena, CA 91125, USA
[5] Núcleo de Astronomía de la Facultad de Ingeniería y Ciencias, Universidad Diego Portales, Av. Ejército Libertador 441, Santiago, Chile
[6] Chinese Academy of Sciences South America Center for Astronomy, National Astronomical Observatories, CAS, Beijing 100101, People's Republic of China
[7] Institute of Astrophysics, Foundation for Research and Technology-Hellas, GR-71110, Heraklion, Greece
[8] Hiroshima Astrophysical Science Center, Hiroshima University, 1-3-1 Kagamiyama, Higashi-Hiroshima, Hiroshima 739-8526, Japan
[9] Department of Physics & Astronomy, Clemson University, 118 Kinard Laboratory, Clemson, SC 29634, USA
[10] Department of Physics and Astronomy, University of California, Irvine, 4129 Frederick Reines Hall, Irvine, CA 92697, USA
[11] Department of Physics, University of Crete, Heraklion, 71003, Greece
[12] National Radio Astronomy Observatory, P.O. Box O, Socorro, NM 87801, USA
Received 2021 February 11; revised 2021 May 21; accepted 2021 May 25; published 2021 July 29

Abstract

Nuclear rings are excellent laboratories for studying intense star formation. We present results from a study of nuclear star-forming rings in five nearby normal galaxies from the Star Formation in Radio Survey (SFRS) and four local LIRGs from the Great Observatories All-sky LIRG Survey at sub-kiloparsec resolutions using Very Large Array high-frequency radio continuum observations. We find that nuclear ring star formation (NRSF) contributes 49%–60% of the total star formation of the LIRGs, compared to 7%–40% for the normal galaxies. We characterize a total of 57 individual star-forming regions in these rings, and find that with measured sizes of 10–200 pc, NRSF regions in the LIRGs have star formation rate (SFR) and $\Sigma_{\rm SFR}$ up to 1.7 $M_\odot$ yr^{-1} and 402 $M_\odot$ yr^{-1} kpc^{-2}, respectively, which are about 10 times higher than in NRSF regions in the normal galaxies with similar sizes, and comparable to lensed high-z star-forming regions. At ∼100–300 pc scales, we estimate low contributions (<50%) of thermal free–free emission to total radio continuum emission at 33 GHz in the NRSF regions in the LIRGs, but large variations possibly exist at smaller physical scales. Finally, using archival sub-kiloparsec resolution CO ($J = 1$–0) data of nuclear rings in the normal galaxies and NGC 7469 (LIRG), we find a large scatter in gas depletion times at similar molecular gas surface densities, which tentatively points to a multimodal star formation relation on sub-kiloparsec scales.

Unified Astronomy Thesaurus concepts: Star forming regions (1565); Luminous infrared galaxies (946); Galaxy structure (622); Radio continuum emission (1340); Galaxy nuclei (609)

1. Introduction

At least one fifth of disk galaxies host star-forming nuclear rings (Knapen 2005). It is commonly accepted that nuclear rings result from a nonaxisymmetric gravitational potential in galaxy centers, which can be induced by the presence of a stellar bar, strong spiral arms, or tidal interaction (e.g., Combes & Gerin 1985; Shlosman et al. 1990; Athanassoula 1994; Buta & Combes 1996; Combes 2001). Such nonaxisymmetry can drive large amounts of gas into the central region and eventually develop a ring of dense gas and intense star formation (SF) surrounding the galactic nucleus, likely at the location of the inner Lindblad resonance (Kim & Stone 2012; Li et al. 2015) or nuclear Lindblad resonance (Fukuda et al. 1998). Optical and infrared (IR) studies of nuclear rings in nearby galaxies indicate that they are prolific in producing young (<100 Myr) and massive (∼10^5 $M_\odot$) star clusters in episodic starbursts (e.g., Maoz et al. 1996; Buta et al. 2000; Maoz et al. 2001). With large reservoirs of dense gas present, nuclear rings are predicted to be long-lived despite the enhanced massive SF (Barreto et al. 1991; Regan & Teuben 2003; Allard et al. 2006; Sarzi et al. 2007). Simulations have been used to predict that even when subject to supernovae feedback, nuclear rings may persist on gigayear timescales (Knapen et al. 1995; Seo & Kim 2013, 2014). Therefore, nuclear rings provide excellent opportunities to study extreme cases of SF in nearby systems.

As a result of long-lasting SF activity, nuclear rings can account for a large fraction of the stellar mass and bolometric luminosity in their host galaxies (e.g., Barreto et al. 1991; Genzel et al. 1995). In the process of secular evolution, nuclear ring SF (NRSF) often emerges as galactic pseudo-bulges slowly assemble from disk material (Kormendy & Kennicutt 2004). Meanwhile, powerful NRSF has also been seen in high-resolution observations of galaxy mergers (e.g., Genzel et al. 1995; Knapen et al. 2004; Haan et al. 2013; Herrero-Illana et al. 2014), which is a comparatively more dramatic evolutionary process. Simulations of galaxy mergers have also proposed nuclear rings as a potential fueling mechanism of quasars (Hopkins & Quataert 2010). Therefore formation of nuclear rings may represent a common and critical phase in galaxy evolution, and properties of NRSF may provide insights into the key dynamical processes associated with various evolutionary paths.

While nuclear rings in nearby disk galaxies have been extensively investigated in the optical and IR, studies of nuclear rings in galaxy mergers are relatively scarce, making a consistent comparison of the two galaxy populations difficult.

Luminous and ultraluminous infrared galaxies (LIRGs: $L_{\rm IR}(8\text{–}1000\,\mu{\rm m}) > 10^{11}\ L_{\odot}$; ULIRGs: $L_{\rm IR}(8\text{–}1000\,\mu{\rm m}) > 10^{12}\ L_{\odot}$) in the local universe, which are often interacting or merging gas-rich spirals, have provided excellent opportunities to study SF in mergers. However, heavy dust obscuration makes the centers of these systems elusive at optical wavelengths (Sanders & Mirabel 1996). Meanwhile, measurements of the nuclei in U/LIRGs can still be heavily affected by nonuniform dust extinction even in the IR (Díaz-Santos et al. 2011; Piqueras López et al. 2013; U et al. 2019).

With the advancement of high-frequency radio interferometry, a highly detailed, extinction-free view of the heavily obscured hearts of local LIRGs becomes possible. In the present study, we make use of high-resolution (∼100 pc) Very Large Array (VLA) observations to characterize and compare the SF properties of nuclear rings hosted in five normal disk galaxies and four LIRGs in the local universe. Observations of these LIRGs are part of a new VLA campaign for the Great Observatories All-sky LIRG Survey (GOALS; Armus et al. 2009), which contains 68 local U/LIRGs, and the normal galaxies are observed with the Star Formation in Radio Survey (SFRS; Murphy et al. 2012, 2018; Linden et al. 2020) of 56 nearby normal star-forming disk galaxies. These two projects together provide a direct, high-resolution comparison of SF activity in interacting and isolated galaxies in the local universe. In this paper, we focus on comparing properties of NRSF observed in these two surveys using high-frequency radio continuum as an extinction-free tracer. A full study of the nuclear SF properties in the GOALS VLA campaign will be presented in a forthcoming paper.

This paper is divided into seven sections. We present our sample selection, observations, and calibration procedures in Sections 2 and 3. In Section 4, we describe the measurements we perform to characterize the properties of the nuclear rings and the individual NRSF regions, the results of which are presented in Section 5. In Section 6, we discuss the limitations and implications of the results. Finally, Section 7 summarizes major findings and conclusions.

Throughout this work we adopt $H_0 = 70$ km s^{-1} Mpc^{-1}, $\Omega_{\rm matter} = 0.28$, and $\Omega_{\Lambda} = 0.72$ based on the five-year result from the Wilkinson Microwave Anisotropy Probe (Hinshaw et al. 2009). These parameters are used with the three-attractor model (Mould et al. 2000) to calculate the luminosity distances and physical scales of the LIRGs in the sample.

2. Sample Selection

The GOALS "equatorial" VLA campaign (Linden et al. 2019; Y. Song et al. in preparation) is a multifrequency, multiresolution snapshot survey designed to map the brightest radio continuum emission in all 68 U/LIRGs from GOALS that are within decl. $|\delta| < 20°$ at Ka (33 GHz), Ku (15 GHz), and S (3 GHz) bands at kiloparsec and ∼100 pc scales. These observations serve as a companion to SFRS, which imaged 56 nearby ($D_L < 30$ Mpc) normal star-forming galaxies (i.e., non-U/LIRGs) from SINGS (Kennicutt et al. 2003) and KINGFISH (Kennicutt et al. 2011) at matched frequencies and also at both kiloparsec (Murphy et al. 2012) and ∼100 pc scales (Murphy et al. 2018; Linden et al. 2020). Using the kiloparsec resolution observations from the GOALS equatorial survey, Linden et al. (2019) studied extranuclear star formation in 25 local LIRGs, and concluded that the high global SFR of these systems, relative to the star formation main sequence (e.g., Elbaz et al. 2011; Speagle et al. 2014) occupied by normal galaxies in SFRS, must be driven by extreme nuclear SF.

In this work we focus on studying and comparing star-forming properties of nuclear rings at ∼100 pc scales in a sample of nine galaxies in SFRS and GOALS. While the term "nuclear ring" is traditionally reserved for rings forming at the nuclear Lindblad resonance (Fukuda et al. 1998), it has also been more broadly used to describe the innermost star-forming rings in galaxies (e.g., Böker et al. 2008). In this paper, we follow the definition and size measurements given in a study of 113 nearby nuclear rings by Comerón et al. (2010), and use "nuclear ring" to describe ring-like emission within the central 2 kpc of a galaxy detected in our surveys at 3, 15, or 33 GHz in radio continuum. With the exceptions of the rings in NGC 1797 and NGC 7591, which are resolved for the first time with the GOALS equatorial survey, all other rings reported here have previously been identified and separately studied as "nuclear rings" at various wavelengths (e.g., Mazzuca et al. 2008; Comerón et al. 2010; Ma et al. 2018). In some other studies, these rings have also been referred to as "circumnuclear rings" (e.g., Xu et al. 2015; Prieto et al. 2019). Figures 1(a) and (b) show the VLA images of the sample, and Table 1 lists the basic properties of the host galaxies.

We note that due to the sensitivity limit of our VLA observations, we were only able to identify the nine nuclear rings that show consistently bright ($\gtrsim$0.1 mJy beam^{-1}) high-frequency (15 or 33 GHz) emission among the combined total of 124 targets from SFRS and the GOALS equatorial survey. Several other galaxies, such as NGC 1068 (LIRG) and NGC 5194 (normal), are also known nuclear ring hosts from optical studies (e.g., Telesco & Decher 1988; Laurikainen & Salo 2002), but their ring structures were not detected in our observations. We further discuss the potential biases of the sample selection in Section 6.1.

3. Observations and Data Reduction

3.1. VLA Data

Each galaxy was observed with the VLA at S (3 GHz), Ku (15 GHz), and Ka (33 GHz) bands. Observations of the five normal galaxies are acquired from the SFRS. This survey observed all galaxies at S, Ku, and Ka bands in B, C, and D configurations, respectively, to achieve a common angular resolution of ∼2.″0 at each frequency. Details of SFRS observations and data calibration procedures are described in Murphy et al. (2018) and Linden et al. (2020).

The four LIRGs were observed with both A (0.″06–0.″6) and C (0.″6–7.″0) configurations at 3, 15, and 33 GHz. The observations were carried out with projects VLA/14A-471 (PI: A. Evans) and VLA/16A-204 (PI: S. Linden). The raw VLA data sets were first reduced and calibrated with the standard calibration pipelines using the Common Astronomy Software Applications (CASA, v4.7.0; McMullin et al. 2007). Each measurement set was visually inspected, and data related to bad antennas, time, and frequency ranges (including radio-frequency interference) were manually flagged. The above two steps were repeated until all bad data were removed.

Before imaging, we performed data combination on the reduced A and C configuration measurement sets at each frequency using CASAv4.7.0 `concat` task with a weighting scale of 100:1 (A:C). This was done to enhance the image sensitivity while maximizing resolution, as well as maintaining good shapes of the point-spread function (i.e., Gaussian-like), accounting for the fact that the

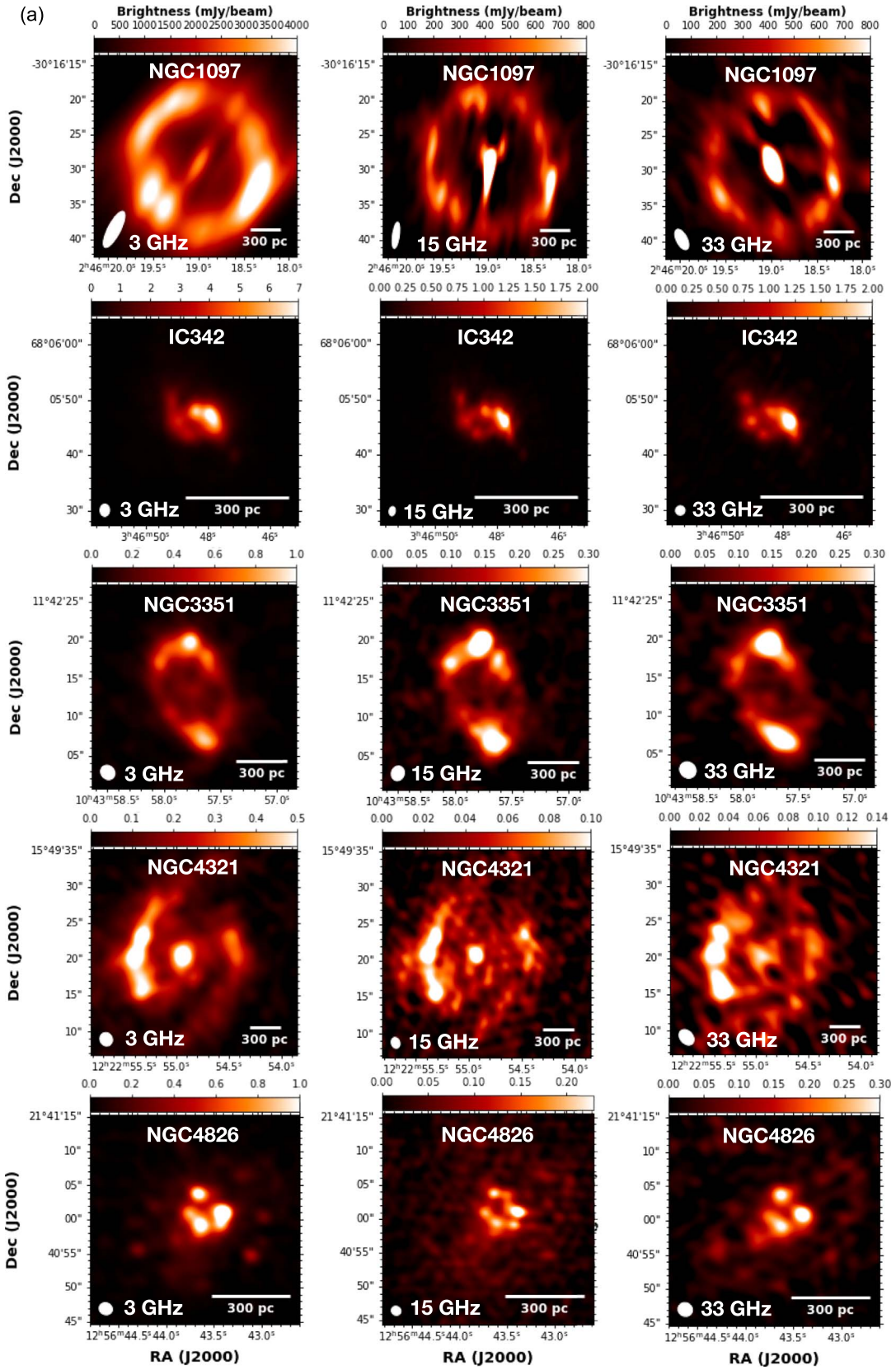

Figure 1. (a) Highest-resolution Ka, Ku, and S band images of the five nuclear rings hosted in the normal galaxies from SFRS. Each image is displayed with bilinear interpolation, in units of mJy beam^{-1}, and the synthesized beam is represented by the white filled ellipse in the lower left corner. The nuclear rings are well detected and resolved at all three bands. (b) Highest-resolution Ka, Ku, and S band images for the four nuclear rings hosted in LIRGs from GOALS. Each image is displayed with bilinear interpolation, in units of mJy beam^{-1}, and the synthesized beam is represented by the white filled ellipse in the lower left corner. All rings are detected and resolved at all three bands except for NGC 7591, whose nuclear ring was only resolved at Ku band.

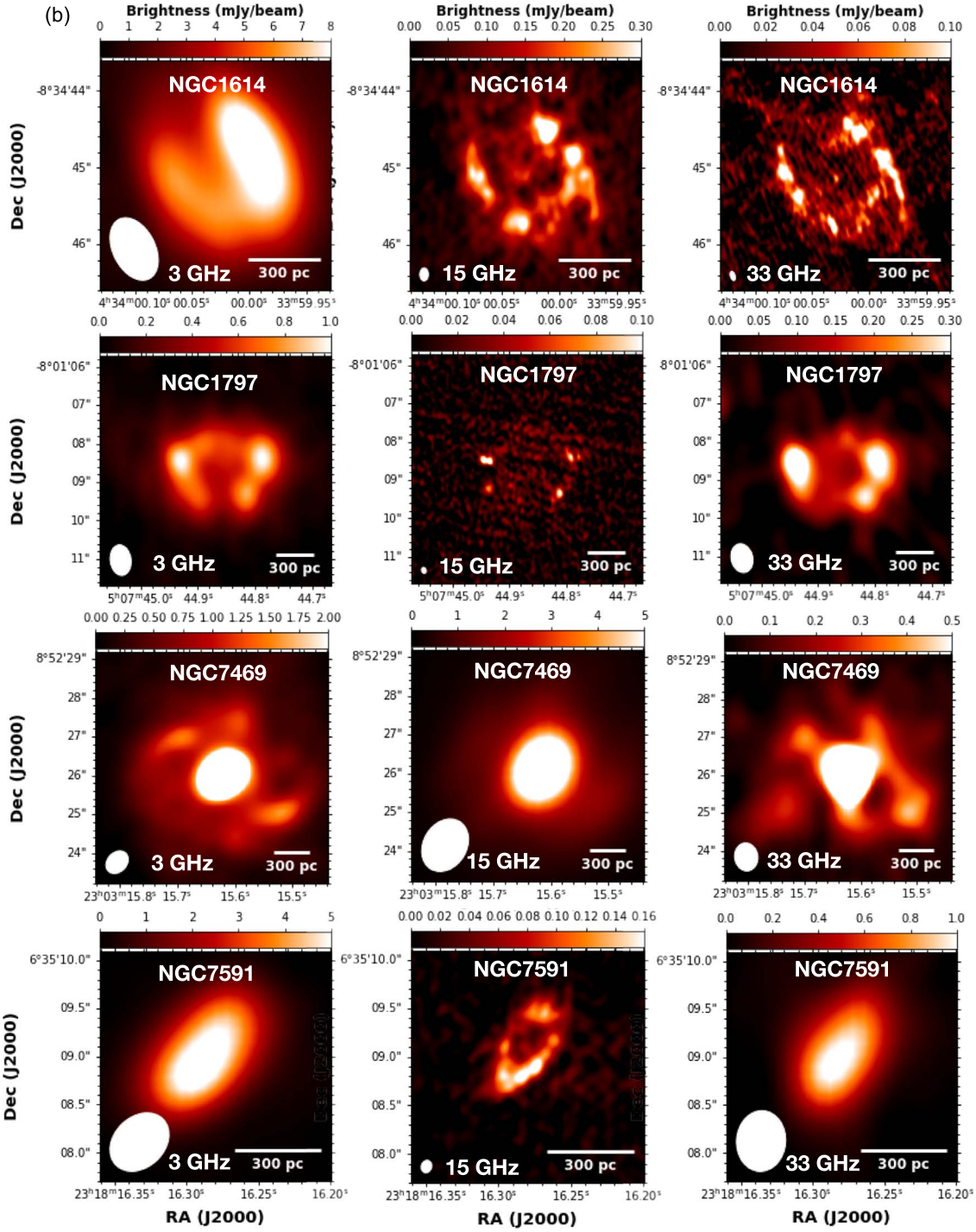

Figure 1. (Continued.)

uv-plane distribution of C configuration data is ∼100 times denser than A configuration. The concatenated measurement sets were then imaged using CASAv4.7.0 `tclean` task, using Briggs weighting with a robust parameter of 1.0 and a (multiscale) multifrequency synthesis deconvolving algorithm.

Due to short on-source times, high-resolution A configuration imaging is unable to recover the nuclear ring emission at 33 GHz for NGC 1797 and NGC 7591, and at both 15 and 33 GHz for NGC 7469. Therefore, in these cases, we use images made from C configuration measurement sets only, using the same `tclean` parameters as above. Additionally, bright nuclear emission in NGC 7469 allowed for self-calibration of the C configuration data at 3, 15, and 33 GHz. Native resolution images of all data referred to in this work are displayed in Figures 1(a) and (b), and descriptions of these images and extra information on individual sources are provided in Appendix A. The characteristics of these images and associated observation information are listed in Table 2.

3.2. Archival CO (J = 1–0) Data

To better understand the properties of star formation in nuclear rings, it is informative to study the molecular environments that

Table 1
Properties of Sample Galaxies

Host	R.A. (J2000)	Decl. (J2000)	D_L (Mpc)	$\log_{10}(L_{IR}/L_\odot)$	Scale (pc arcsec^{-1})	Type	f_{AGN}^{bol} (%)	Survey	Morphology	Merger Stage
(1)	(2)	(3)	(4)	(5)	(6)	(7)	(8)	(9)	(10)	(11)
NGC 1097	$02^h46^m19^s.0$	$-30^d16^m30^s$	14.2	10.56	69	LINER/Sy1	⋯	SFRS	SBb	N*
IC 342	$03^h46^m48^s.5$	$+68^d05^m47^s$	3.3	9.87	16	H II	⋯	SFRS	SABcd	N
NGC 3351	$10^h43^m57^s.7$	$+11^d42^m14^s$	9.3	9.77	45	H II	⋯	SFRS	SBb	N
NGC 4321	$12^h22^m54^s.8$	$+15^d49^m19^s$	14.3	10.33	70	H II/LINER	⋯	SFRS	SABbc	N
NGC 4826	$12^h56^m43^s.6$	$+21^d40^m59^s$	5.3	9.54	26	LINER	⋯	SFRS	SAab	N
NGC 1614	$04^h33^m59^s.8$	$-08^d34^m44^s$	67.8	11.65	323	H II	12 ± 8	GOALS	SBc pec	d
NGC 1797	$05^h07^m44^s.9$	$-08^d01^m09^s$	63.4	11.04	303	H II	6 ± 3	GOALS	SBa pec	a
NGC 7469	$23^h03^m15^s.6$	$+08^d52^m26^s$	70.8	11.58	332	Sy1	24 ± 6	GOALS	SABa	a
NGC 7591	$23^h18^m16^s.3$	$+06^d35^m09^s$	71.4	11.12	335	LINER	9 ± 2	GOALS	SBbc	N

Note. (1) Host galaxy of the nuclear ring. (2) and (3) Coordinates of the host galaxy. (4) Distance to the host galaxy. For SFRS galaxies, we use redshift-independent distances reported in Kennicutt et al. (2011). For GOALS galaxies, we use luminosity distances reported in Armus et al. (2009), where they adopted the three-attractor model (Mould et al. 2000). (5) Total infrared luminosity (8–1000 μm) of the host galaxy in solar units ($L_\odot = 3.826 \times 10^{33}$ erg s^{-1}), calculated using distances from (4) and IRAS flux densities in Sanders et al. (2003) with recipes given in Sanders & Mirabel 1996. NGC 7469 is in a close interacting pair, so we use instead the value for the resolved major component from Howell et al. (2010). (6) Angular to physical scale conversion factor. For LIRGs, this is calculated using Ned Wright's Cosmology Calculator (Wright 2006) in combination with the three-attractor model (Mould et al. 2000). (7) References for active type classification: NGC 1097: Phillips et al. (1984), Storchi-Bergmann et al. (1993); NGC 3351: Planesas et al. (1997); NGC 4321: Ho et al. (1997); NGC 4826: García-Burillo et al. (2003); NGC 1614: Herrero-Illana et al. (2017); NGC 1797: Balzano (1983); NGC 7469: Osterbrock & Martel (1993); NGC 7591: Pereira-Santaella et al. (2010). (8) AGN contribution to the bolometric luminosity of the host galaxy, estimated by Díaz-Santos et al. (2017) for the GOALS galaxies using five different mid-IR AGN diagnostics. The AGN contribution to the bolometric light is expected to be negligible in the SFRS galaxies (e.g., Dale et al. 2009). (9) Survey with which nuclear ring observations were taken. (10) Morphology classification of the host galaxy from the NASA/IPAC Extragalactic Database (NED). (11) Merger stages for the GOALS galaxies are determined by Stierwalt et al. (2013) via visual inspection of the Spitzer IRAC 3.6 μm observations (N = non-merger, a = pre-merger, d = late-merger). Using the same criteria, we classify all SFRS galaxies as non-mergers, given the lack of massive neighbors in their proximity. *However, NGC 1097 is actively interacting with at least one dwarf companion (Bowen et al. 2016).

give rise to this activity. For each host galaxy in the sample, we searched for archival CO ($J = 1$–0) observations with resolutions that are comparable to or higher than our VLA observations to directly compare SF and the properties of cold molecular gas in its nuclear ring. Four galaxies in our sample have publicly available archival Atacama Large Millimeter/submillimeter Array (ALMA) data that meet the above criteria, from ALMA projects 2012.1.00001.S (NGC 1097, PI: K. Sheth; unpublished), 2013.1.00885.S (NGC 3351, PI: K. Sandstrom; Leaman et al. 2019), 2015.1.00978.S (NGC 4321, PI: K. Sandstrom; unpublished), 2016.1.00972.S (NGC 4321, PI: K. Sandstrom; unpublished), and 2013.1.00218.S (NGC 7469, PI: T. Izumi; Zaragoza-Cardiel et al. 2017; Wilson et al. 2019). Each ALMA data set was first reprocessed using the appropriate CASA version and data calibration pipeline that are specified in the project's data calibration note from the archive. Continuum subtraction was performed using the `uvcontsub` task in CASA (version consistent with reduction pipeline). The reduced measurement sets were then reimaged using `tclean` in CASAv4.7.0, using Briggs weighting with a robust parameter of 0.5 and the Högbom cleaning algorithm. For NGC 1097, because the native angular resolution of the data set is about four times higher than that of the VLA data, we also tapered the *uv*-distribution of the measurement sets with a 3.″0 Gaussian kernel to better compare with the VLA data. We then produced moment 0 maps from the continuum-subtracted CO ($J = 1$–0) line cubes using the `immoments` task in CASAv4.7.0.

Additionally, we downloaded high-resolution CO ($J = 1$–0) moment 0 maps for NGC 4826 (Casasola et al. 2015) and IC 342 (Ishizuki et al. 1990) from NED. The map for NGC 4826 was observed by the IRAM Plateau de Bure Interferometer (PdBI), and provided in units of $M_\odot$ pc^{-2}. We used information from Table 1 and Equation (2) in Casasola et al. (2015) to convert the data to units of Jy beam^{-1} km s^{-1}. The map for IC 342 was observed using the 10 m submillimeter telescope (NRO10m) at Nobeyama Radio Observatory, and provided in units of Jy beam^{-1} m s^{-1} in B1950 coordinates. We used the `imregrid` task in CASA to remap the data sets to match the coordinates of our VLA data (J2000), after which we converted the data to units of Jy beam^{-1} km s^{-1}.

Characteristics of these moment 0 maps are listed in Table 3. In Section 4.3, we utilize these moment 0 maps to estimate the cold molecular gas densities and gas depletion times in these six nuclear rings.

4. Data Analysis

Here we mainly use the 33 GHz continuum images for our analysis of the nuclear rings and individual NRSF regions because radio continuum emission above 30 GHz has been shown to effectively trace thermal free–free emission associated with ongoing massive SF in both normal galaxies and LIRGs (e.g., Murphy et al. 2012; Linden et al. 2019, 2020). For NGC 7591, we use the 15 GHz image instead because the available 33 GHz image does not resolve the ring structure.

4.1. Integrated Ring Measurements

To measure the integrated ring properties, we first quantify the spatial extent of each ring by defining inner, peak, and outer radii/semimajor axes (R_{in}, R_{peak}, R_{out}) based on its azimuthally averaged light profile, as shown in Figure 2. These light profiles are measured from the central coordinates of the host galaxies using 1 pixel wide circular annuli. Elliptical annuli are used for highly elliptical rings (NGC 3351, NGC 1797, and NGC 7591). Details of the relevant procedures are provided in Appendix B. In general, we locate R_{in} at the first local minimum of the light profile, and define R_{peak} at the local maximum outside R_{in}. To account for diffuse emission from the ring that is not necessarily axisymmetric, we define R_{out} to be where the averaged light

Table 2
Observations and Image Characteristics of VLA Data

Galaxy	Project ID	Band	Configuration	Beam	PA (deg)	Physical Resolution[b] (pc)	$\sigma_{\rm rms}$ (μJy beam^{-1})
NGC 1097	11B-032	Ka	D	$3\farcs17 \times 1\farcs55$	26.7	107	40.4
	13B-215	Ku	C	$3\farcs81 \times 0\farcs99$	−7.6	69	20.0
	13B-215	S	B	$5\farcs76 \times 1\farcs80$	−27.4	125	46.3
IC 342	11B-032	Ka	D	$1\farcs76 \times 1\farcs72$	−34.3	28	35.2
	13B-215	Ku	C	$1\farcs72 \times 1\farcs13$	−9.5	18	15.1
	13B-215	S	B	$2\farcs23 \times 1\farcs76$	−0.8	28	38.5
NGC 3351	11B-032, 13A-129	Ka	D	$2\farcs27 \times 2\farcs04$	47.2	92	17.2
	13B-215	Ku	C	$1\farcs95 \times 1\farcs67$	−17.5	75	14.1
	13B-215	S	B	$2\farcs01 \times 1\farcs75$	43.6	79	17.2
NGC 4321	13A-129	Ka	D	$2\farcs41 \times 1\farcs77$	42.3	123	18.5
	13B-215	Ku	C	$1\farcs53 \times 1\farcs17$	17.0	82	9.7
	13B-215	S	B	$1\farcs89 \times 1\farcs72$	30.6	120	15.0
NGC 4826	13A-129	Ka	D	$2\farcs16 \times 1\farcs98$	65.9	51	13.4
	13B-215	Ku	C	$1\farcs46 \times 1\farcs33$	61.3	34	10.4
	13B-215	S	B	$1\farcs97 \times 1\farcs75$	67.3	45	14.0
NGC 1614	14A-471, 16A-204	Ka	A,C	$0\farcs12 \times 0\farcs06$	16.8	19	13.5
	14A-471	Ku	A,C	$0\farcs17 \times 0\farcs11$	−0.4	36	18.8
	14A-471	S	A,C	$0\farcs87 \times 0\farcs55$	26.8	178	12.3
NGC 1797	14A-471	Ka	C	$0\farcs76 \times 0\farcs56$[a]	13.7	170	16.5
	14A-471	Ku	A,C	$0\farcs13 \times 0\farcs12$	15.6	36	10.0
	14A-471	S	A,C	$0\farcs80 \times 0\farcs54$	7.6	164	19.4
NGC 7469	14A-471	Ka	C	$0\farcs63 \times 0\farcs52$[a]	2.4	173	21.1
	14A-471	Ku	C	$1\farcs44 \times 1\farcs12$[a]	−30.8	372	13.5
	14A-471	S	A,C	$0\farcs65 \times 0\farcs50$	−43.4	166	40.2
NGC 7591	14A-471	Ka	C	$0\farcs63 \times 0\farcs51$[a]	−4.1	171	17.9
	14A-471	Ku	A,C	$0\farcs13 \times 0\farcs11$	−17.6	37	9.4
	14A-471	S	A,C	$0\farcs68 \times 0\farcs54$	−50.7	181	27.9

Notes. The central frequencies for Ka, Ku, and S bands are 33 GHz, 15 GHz, and 3 GHz, respectively. The rms error $\sigma_{\rm rms}$ was measured manually on each image before primary beam correction in an emission-free region. A and C configuration data sets are weighted with 100:1 (A:C) before combined imaging to account for differences in *uv*-plane distribution. PA is position angle.
[a] C configuration image was used due to limited dynamic range at A configuration.
[b] The smallest physical scale resolved by the synthesized beam at the distance of the galaxy, given the FWHM of the minor axis of the beam.

profile flattens toward the image noise level (i.e., $\sigma_{\rm rms}$ in Table 2). An exception to this is NGC 4826, whose averaged light profile contains a contribution from a faint spiral structure that surrounds the ring, which we exclude from further analysis by setting $R_{\rm out}$ at the local minimum immediately outside $R_{\rm peak}$. Due to the limited resolution of the observations, light profiles of IC 342, NGC 4826, and NGC 1797 do not yield a well defined local minimum, therefore we do not use $R_{\rm in}$ for rings in these three galaxies. See Appendix A for more details of individual sources.

The flux of each ring is then measured within the area characterized by $R_{\rm in}$ and $R_{\rm out}$ via aperture photometry. For NGC 4826, a LINER active galactic nucleus (AGN) likely contributes to the ring emission due to $m = 1$ perturbation (García-Burillo et al. 2003), therefore we additionally mask the image at the reported AGN location ($\alpha_{\rm J2000} = 12^{\rm h}56^{\rm m}43\overset{\rm s}{.}64$, $\delta_{\rm J2000} = 21^{\rm d}40^{\rm m}59\overset{\rm s}{.}30$) with a beam-sized aperture before performing aperture photometry. In Figure 2, we also mark the locations of known AGNs with "+". We do not find similar cases of AGN emission contributing to the nuclear ring in the rest of the sample.

4.2. NRSF Region Identification and Measurements

Given the high resolution of our VLA observations, all nine nuclear rings are resolved at sub-kiloparsec scales at 33 GHz or 15 GHz, thus allowing us to further characterize the properties of individual star-forming regions in these rings.

To identify and measure the flux of individual NRSF regions in each nuclear ring, we use the software Astrodendro (Robitaille et al. 2019), which measures hierarchical structures in an astronomical image using dendrograms. Astrodendro identifies and categorizes structures in an image into `trunk`, `branch`, and `leaf`, based on three input parameters: the minimum brightness required for a structure to be physically meaningful (`min_value`), the minimum number of pixels in a structure (`min_npix`), and the minimum brightness relative to the local background required for a structure to be considered independent (`min_delta`). Structures identified as `leaf` are of the highest hierarchical order, and are the individual NRSF regions that we are interested in, while `branch` and `trunk` are the less luminous diffuse ring emission connecting the SF regions. Therefore here we only focus on the derived properties of `leaf` structures.

We run Astrodendro on the 33 GHz image of each nuclear ring (15 GHz for NGC 7591) with `min_value` $= 5\sigma_{\rm rms}$ and `min_delta` $= 1\sigma_{\rm rms}$ to identify physically meaningful `leaf` structures, where $\sigma_{\rm rms}$ is the rms noise measured in an emission-free region of the image before primary beam correction (see Table 2). We set `min_npix` to be 1/4 the area of the synthesized beam, to avoid identifying noise spikes yet to allow detection of small, unresolved regions. Afterwards, we manually eliminate regions identified beyond the outer radius ($R_{\rm out}$) of the ring to ensure we only include NRSF regions or nuclei in subsequent analyses. Figure 3 shows all the

Table 3
Observations and Image Characteristics of Ancillary CO ($J = 1$–0) Data

Galaxy	Telescope	Project ID/Reference	Beam	PA (deg)	Physical Resolution[a] (pc)	$\sigma_{\rm rms}$ (mJy beam^{-1} km s^{-1})
NGC 1097	ALMA	2012.1.00001.S	$2\farcs85 \times 2\farcs57$	72.6	178	2.8
IC 342	NRO10m	Ishizuki et al. (1990)	$2\farcs39 \times 2\farcs27$	−31	36	3.5
NGC 3351	ALMA	2013.1.00885.S	$2\farcs03 \times 1\farcs22$	27.8	55	0.5
NGC 4321	ALMA	2015.1.00978.S	$2\farcs40 \times 2\farcs24$	−31.0	156	0.4
	ALMA	2016.1.00972.S				
NGC 4826	IRAM	Casasola et al. (2015)	$2\farcs53 \times 1.\farcs80$	39.0	156	0.25
NGC 7469	ALMA	2013.1.00218.S	$0\farcs91 \times 0\farcs51$	−48.8	169	0.2

Note. For NGC 4321, we combined the measurement sets from two different ALMA projects to produce CO ($J = 1$–0) moment 0 maps. For ALMA data sets, the rms error $\sigma_{\rm rms}$ was measured manually on each continuum-subtracted line cube before primary beam correction in an emission-free region across all channels. For NGC 4826 and IC 342, $\sigma_{\rm rms}$ was taken from the original references. ALMA data sets for NGC 1097 and NGC 4321 are unpublished. The data set for NGC 3351 is published in Leaman et al. (2019), and that for NGC 7469 is published in Zaragoza-Cardiel et al. (2017) and Wilson et al. (2019).
[a] The smallest physical scale resolved by the synthesized beam at the distance of the galaxy, given the FWHM of the minor axis of the beam.

regions identified using Astrodendro. We note that varying `min_npix` by small amounts does not significantly alter the population of identified `leaf` structures. For example, setting `min_npix` to be 1/2 or 3/4 of the beam area only blends together Regions 1 and 3 in NGC 1797, and Regions 3 and 6 in NGC 7469, and the rest of the region identification remains exactly the same in terms of numbers, sizes, and shapes.

The flux density and angular area of each identified region are also measured by Astrodendro, and can be heavily dependent on the signal-to-noise ratio (S/N) of the region. To characterize the effect of image noise on the region size and flux measurements, we use a Monte Carlo method and rerun Astrodendro 1000 times, randomly adjusting the brightness of each pixel sampling from a Gaussian distribution defined by the rms noise $\sigma_{\rm rms}$ and the assumed VLA flux calibration error ($\sim$10%). The standard deviations of the results from the 1000 runs are used to quantify the uncertainties in the flux and size measurements. For unresolved regions that have Astrodendro-measured sizes smaller than the beam areas after accounting for uncertainties, we instead measure their flux using beam-sized apertures and use the beam areas as upper limits for their sizes.

Additionally, to estimate the ratio of thermal free–free emission to total radio continuum emission in these NRSF regions at 33 GHz, we measure the radio spectral index between 15 and 33 GHz associated with each region. To do so, we smooth and regrid the native resolution 15 GHz and 33 GHz images of each nuclear ring (shown in Figures 1(a) and (b)) to a common circular beam and pixel scale for consistent measurements of flux densities across the two frequencies. Assuming a single power-law model representing the combination of flat-spectrum thermal emission and steep-spectrum nonthermal emission $S \sim \nu^{\alpha}$, we can calculate the spectral index α associated with each region by measuring the linear slope between flux densities measured at 15 and 33 GHz with respect to frequency. Due to the coarser resolutions of the beam-matched images, the exact region areas identified with Astrodendro using native resolution images cannot be used here to extract spectral indices. As an approximation, for each region we measure its beam-matched 15 and 33 GHz flux using a common circular aperture with area equivalent to the region size as measured by Astrodendro. For regions with sizes smaller than the matched circular beams, we instead use beam-sized apertures to extract their associated spectral indices. Uncertainties in the spectral indices are calculated with error propagation.

4.3. Measurements of CO (J = 1–0) Maps

For the six galaxies that have high-resolution ancillary CO ($J = 1$–0) data (see Section 3.2), we smooth and regrid the native resolution CO ($J = 1$–0) moment 0 map and 33 GHz radio continuum map of the nuclear ring to a common circular beam and pixel scale for consistent flux measurements. We measure the total CO ($J = 1$–0) and 33 GHz continuum flux of each ring using apertures defined by $R_{\rm in}$ and $R_{\rm out}$ (see Section 4.1). These values are used to derive the integrated molecular gas mass, average surface densities, and gas depletion times in the ring in Section 5.5. For individual NRSF regions, we measure the CO ($J = 1$–0) and 33 GHz flux using circular apertures with area equivalent to the region size as measured by Astrodendro. For regions with sizes smaller than the matched circular beams, we use beam-sized apertures instead.

5. Results

Here we describe the results of the above measurements and further derive SFR, SFR surface density, and gas depletion time for each ring as a whole, as well as for individual NRSF regions identified using Astrodendro. We also use the measured 15–33 GHz spectral index to derive the ratio of thermal free–free emission to total radio emission at 33 GHz associated with each NRSF region. The measured and derived quantities for the nuclear rings are summarized in Table 4, and those for individual NRSF regions are reported in Table 6. In total, 63 regions are identified and measured with Astrodendro, as shown in Figure 3, i.e., 57 NRSF regions (22 in normal galaxies and 35 in LIRGs) and six nuclei (five known AGN and one nuclear starburst). For completeness, in Table 6 we report measurements for all 63 identified regions, but only the 57 NRSF regions are included in the final analysis.

5.1. Ring Size, SFR, and SFR Surface Density

We use $R_{\rm peak}$, defined in Section 4.1, as an estimate for the radius/semimajor axis of the ring. The five nuclear rings in the sample of normal galaxies have radii of 43–599 pc, and the four nuclear rings in the LIRGs have radii of 121–531 pc.

Using flux measured with $R_{\rm in}$ and $R_{\rm out}$, we can calculate the integrated SFR within each ring using Equation (10) in

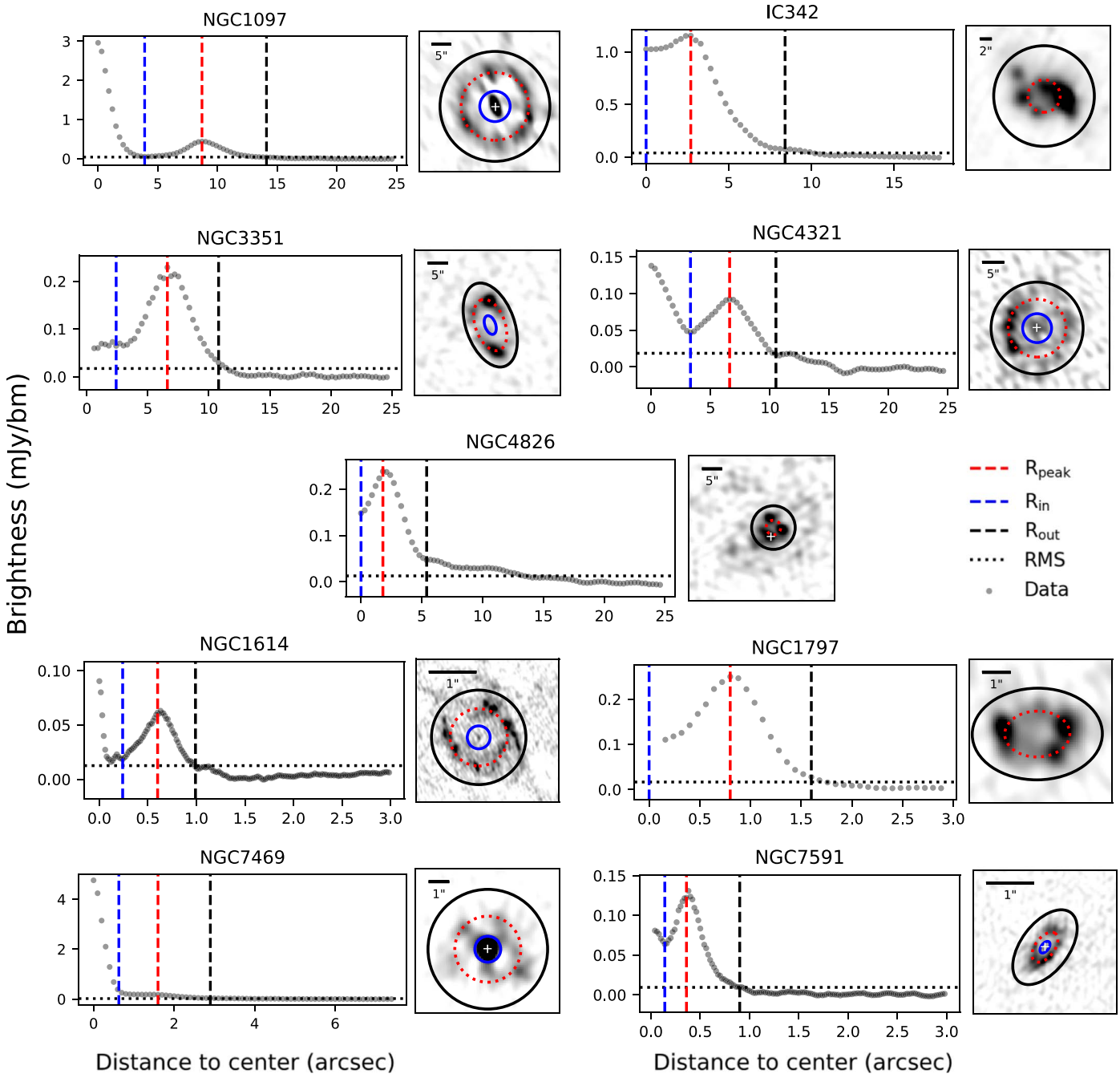

Figure 2. Left column: azimuthally averaged light profile (gray dotted line) from the 33 GHz image of each nuclear ring in the sample. The red dashed vertical line shows the radius of the ring ($R_{\rm peak}$), and the blue and black dashed vertical lines mark the inner and outer radii ($R_{\rm in}$, $R_{\rm out}$), respectively. See Section 4.1 for definitions of the different radii. Right column: 33 GHz image of the nuclear ring shown in grayscale. Circles/ellipses overlaid in dotted red, solid blue, and black mark $R_{\rm peak}$, $R_{\rm in}$, and $R_{\rm out}$, respectively. White "+" signs mark the locations of AGNs. For NGC 7591, observation and measurements at 15 GHz are used here because the available 33 GHz image does not resolve the ring structure.

Murphy et al. (2012):

$$\left(\frac{\rm SFR}{M_\odot\ {\rm yr}^{-1}}\right) = 10^{-27}\left[2.18\left(\frac{T_e}{10^4\ {\rm K}}\right)^{0.45}\left(\frac{\nu}{\rm GHz}\right)^{-0.1} + 15.1\left(\frac{\nu}{\rm GHz}\right)^{\alpha^{\rm NT}}\right]^{-1}\left(\frac{L_\nu}{\rm erg\ s^{-1}\ Hz^{-1}}\right) \quad (1)$$

where a Kroupa initial mass function (IMF) is assumed. In this equation, L_ν is the spectral luminosity at the observed frequency ν, given by $L_\nu = 4\pi D_L^2 S_\nu^r$, where S_ν^r is the measured total flux of the ring in Jy, D_L is the luminosity distance of the host galaxy (column 4 in Table 1), T_e is the electron temperature, and $\alpha^{\rm NT}$ is the nonthermal spectral index. Here we adopt $T_e = 10^4$ K and $\alpha^{\rm NT} = -0.85$, which have been extensively used to describe SF regions in normal galaxies and LIRGs (e.g., Murphy et al. 2012; Linden et al. 2019, 2020).

The integrated SFR has ranges of 0.03–2.0 and 6.1–29 $M_\odot$ yr^{-1} for rings in the normal galaxies and in the LIRGs, respectively. For the normal galaxies, the estimated nuclear

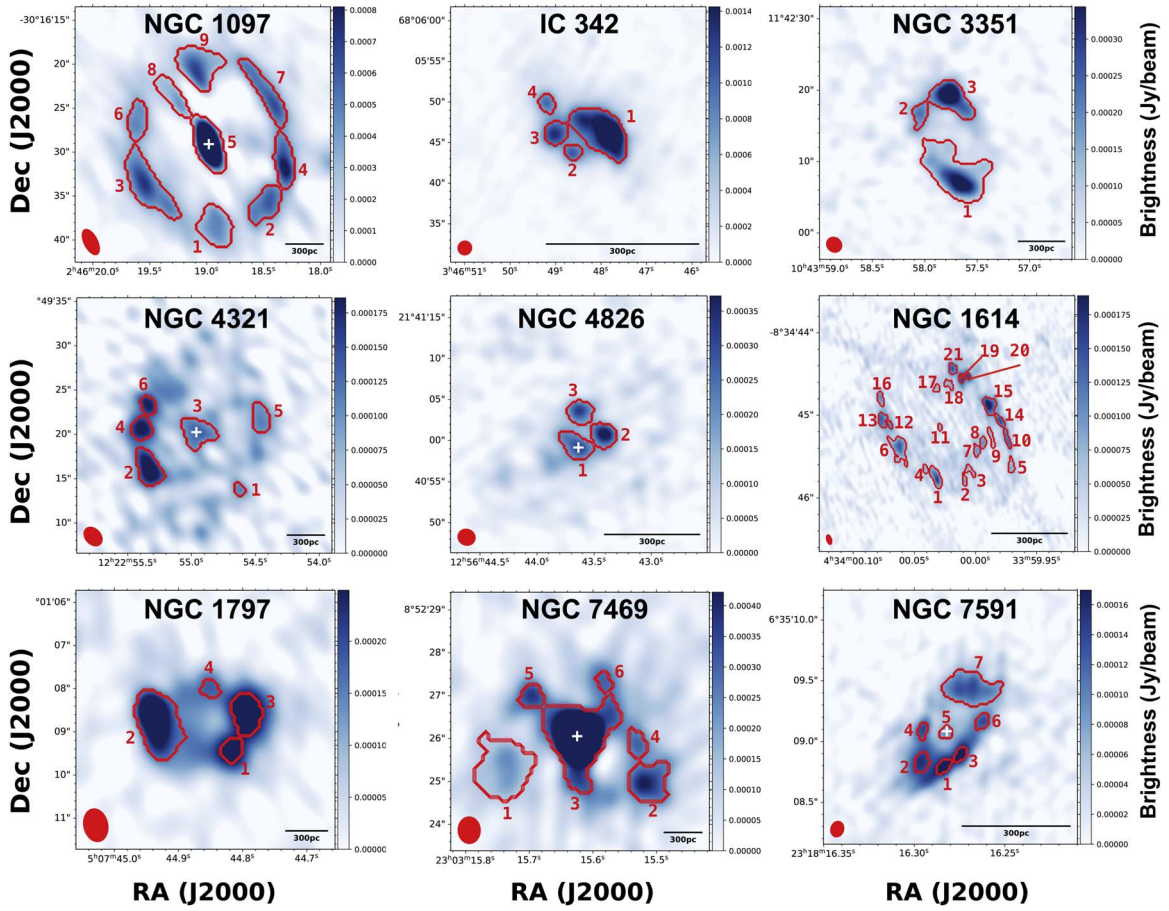

Figure 3. 33 GHz images of the sample galaxies (15 GHz for NGC 7591) with nuclei and NRSF regions identified with Astrodendro outlined in red. Region IDs (labeled in red) are assigned in ascending order based on region declinations. Red ellipses on the bottom left of the images represent the shapes and sizes of synthesized beams. Scale bars shown on the lower right reflect the physical scales of the observed structures at the distance of the host galaxy. White "+" signs mark the locations of known AGNs.

ring radii and SFR are in agreement with previous measurements of the same galaxies at optical and IR wavelengths (e.g., Mazzuca et al. 2008; Comerón et al. 2010; Hsieh et al. 2011; Ma et al. 2018). Only a handful of similar measurements exist for the nuclear rings hosted in LIRGs because they are farther away and more obscured by dust. Our radio measurement is also consistent with extinction-corrected Paα measurement for the nuclear ring in NGC 1614 by Alonso-Herrero et al. (2001), which confirms the effectiveness of using high-frequency radio continuum as an extinction-free SFR tracer in these nuclear rings.

We further calculate the average SFR surface density, $\Sigma_{\rm SFR}$, in each ring, by dividing the integrated SFR by the area of the ring as defined in Figure 2, with $R_{\rm in}$ and $R_{\rm out}$. For rings with undefined $R_{\rm in}$ due to lack of resolution, we use the areas defined by their $R_{\rm out}$ minus the areas of the synthesized beams (Table 2) to account for the central cavities. The resulting range of $\Sigma_{\rm SFR}$ is 0.27–2.90 $M_\odot$ yr^{-1} kpc^{-2} for nuclear rings in the normal galaxies, with a median value of $0.59 \pm 0.21\ M_\odot$ yr^{-1} kpc^{-2}. For rings in the LIRGs, $\Sigma_{\rm SFR}$ is higher by at least a factor of two, with a range of 6.0–97 $M_\odot$ yr^{-1} kpc^{-2} and a median of $30 \pm 22\ M_\odot$ yr^{-1} kpc^{-2}.

5.2. Ring SFR versus Host SFR

Here we estimate the fraction of total SFR of the host galaxy contributed by the nuclear ring. The relevant results are tabulated in Tables 4 and 5. The total SFR of the galaxy is calculated from both far-UV (FUV) and IR emission to account for obscured and unobscured SF (Murphy et al. 2012):

$$\mathrm{SFR_{tot}} = \mathrm{SFR_{FUV}} + \mathrm{SFR_{IR}}. \quad (2)$$

To calculate $\mathrm{SFR_{FUV}}$, we use GALEX FUV measurements from Clark et al. (2018) for the normal galaxies and from Howell et al. (2010) and Brown et al. (2014) for the LIRGs, along with Equation (2) from Murphy et al. (2012) assuming a Kroupa IMF:

$$\mathrm{SFR_{FUV}} = 4.42 \times 10^{-44} L_{\rm FUV}. \quad (3)$$

No GALEX FUV measurements are available for NGC 1614 and NGC 1797. For NGC 1614, SFR based on monochromatic UV measurement ($\lambda = 2800$ Å) is available from U et al. (2012). Due to the different calibrations adopted, UV SFRs from U et al. (2012) are consistently higher than values estimated using FUV measurements from Howell et al. (2010) among U/LIRGs studied in both works, by at least a factor of two. Therefore, for NGC 1614, we adopt here the SFR reported in U et al. (2012), but scaled down by a factor of two as an estimate for its FUV SFR. The FUV contribution to the total SFR is overall very low ($\sim$4%) in local U/LIRGs (Howell et al. 2010) and therefore does not affect our estimates significantly. For the IR component, we applied $L_{\rm IR}$ from Table 1 to Equation (15) in Murphy et al. (2012),

Table 4
Integrated Nuclear Ring Properties

Galaxy	ν (GHz)	R_{in} (pc)	R_{peak} (pc)	R_{out} (pc)	S_ν^r (mJy)	SFR ($M_\odot$ yr^{-1})	Σ_{SFR} ($M_\odot$ yr^{-1} kpc^{-2})	SFR_{ring}/SFR_{tot} (%)
(1)	(2)	(3)	(4)	(5)	(6)	(7)	(8)	(9)
NGC 1097	33	269	599	970	19 ± 2.0	2.0 ± 0.20	0.73 ± 0.07	39 ± 4
IC 342	33	⋯	43	134	29 ± 2.9	0.16 ± 0.02	2.90 ± 0.29	7 ± 1
NGC 3351	33	109	299	489	4.5 ± 0.46	0.20 ± 0.02	0.51 ± 0.05	24 ± 2
NGC 4321	33	229	458	728	3.9 ± 0.42	0.41 ± 0.04	0.27 ± 0.03	13 ± 1
NGC 4826	33	⋯	46	138	2.5 ± 0.26	0.03 ± 0.01	0.69 ± 0.07	7 ± 1
NGC 1614	33	77	194	319	12 ± 1.3	29 ± 3.0	97 ± 9.9	60 ± 8
NGC 1797	33	⋯	242	485	3.0 ± 0.30	6.1 ± 0.63	6.0 ± 0.62	49 ± 5
NGC 7469	33	208	531	963	8.1 ± 0.83	21 ± 2.1	7.6 ± 0.78	57 ± 7
NGC 7591	15	47	121	301	4.2 ± 0.43	8.0 ± 0.82	53 ± 5.3	59 ± 6

Note. (1) Host galaxy of the nuclear ring. (2) Frequency at which sizes and SFR are measured. (3)–(5) inner, peak, and outer radii of the ring, as defined in Section 4.1. Details of individual sources are described in Appendix A. (6) Flux density enclosed by apertures with R_{out} and R_{in}. For NGC 4826, off-centered AGN emission is excluded. (7) Star formation rates calculated using Equation (1) and values from (6). (8) Star formation rate surface densities of each ring, calculated by dividing (7) by the area over which the ring extends. See Section 5.1 for details. (9) Fraction of the total SFR of the host galaxy in the nuclear ring. See Section 5.2 and Table 5 for details.

Table 5
Host Galaxy Star Formation Rates

Galaxy	SFR_{FUV} ($M_\odot$ yr^{-1})	SFR_{IR} ($M_\odot$ yr^{-1})	SFR_{tot} ($M_\odot$ yr^{-1})
(1)	(2)	(3)	(4)
NGC 1097	0.69 ± 0.03	4.4 ± 0.0	5.1 ± 0.0
IC 342	1.50 ± 0.07	0.9 ± 0.0	2.4 ± 0.0
NGC 3351	0.15 ± 0.01	0.7 ± 0.0	0.86 ± 0.01
NGC 4321	0.7 ± 0.03	2.6 ± 0.1	3.3 ± 0.1
NGC 4826	0.04 ± 0.01	0.4 ± 0.0	0.46 ± 0.01
NGC 1614	1.5[a]	47 ± 4.3	48 ± 4
NGC 1797	⋯[a]	12 ± 0.4	12 ± 0.4
NGC 7469	1.7 ± 0.0	37 ± 3.0	39 ± 3
NGC 7591	0.4 ± 0.1	13 ± 0.3	14 ± 0.3

Note. (1) Host galaxy name. (2) Star formation rates derived from GALEX FUV flux measurements by Clark et al. (2018), Howell et al. (2010), and Brown et al. (2014), using Equation (3). (3) Star formation rates derived from total IR luminosity, accounting for the AGN contribution to the bolometric luminosity of the LIRGs (Table 1), using Equation (5). (4) Total star formation rates of the host galaxy. See Section 5.2 for more details.
[a] GALEX measurements are not available for NGC 1614 and NGC 1797. For NGC 1614, we use monochromatic UV SFR from U et al. (2012) scaled down by a factor of two as an estimate for FUV SFR.

modified to account for AGN emission:

$$SFR_{IR} = 3.15 \times 10^{-44} L_{IR,SF} \quad (4)$$

$$= 3.15 \times 10^{-44} L_{IR}(1 - f_{AGN}) \quad (5)$$

where f_{AGN} is the fraction of the bolometric luminosity of the host galaxy contributed by AGN emission (see Table 1 and Díaz-Santos et al. 2017). Because the above relations presented in Murphy et al. (2012) are calibrated against 33 GHz measurements, we can directly estimate the fraction of total SFR contributed by the nuclear ring by dividing the ring SFR, derived in the last section by SFR_{tot}. The fractions are 7%–39% for rings in the normal galaxies, and 49%–60% for rings in the LIRGs, with median values of $12\% \pm 9\%$ and $56\% \pm 6\%$, respectively. We visualize this result in Figure 6 and discuss its implication in Section 6.2. For NGC 1614, a similar fraction has also been estimated by Xu et al. (2015). Even though measurements are made at 15 GHz for NGC 7591, we do not expect new measurements at 33 GHz to significantly alter our result.

5.3. Region Size, SFR, and SFR Surface Density

For each identified NRSF region, we calculate its SFR and Σ_{SFR} using the flux density and area measured in Section 4.2, along with Equation (1). For regions smaller than the beam areas accounting for uncertainties (i.e., unresolved), Σ_{SFR} calculated here are lower limits. To compare the region size with values from the literature, we compute and report the effective radius $R_e = \sqrt{\text{area}/\pi}$, which has a range of 16–184 pc for the 22 NRSF regions in the normal galaxies and 13–221 pc for the 35 NRSF regions in the LIRGs. Regions in the normal galaxies have SFR of 0.01–0.21 $M_\odot$ yr^{-1}, with a median of $0.04 \pm 0.03\ M_\odot$ yr^{-1}. Regions in the LIRGs have SFR of 0.08–1.7 $M_\odot$ yr^{-1}, with a median of $0.25 \pm 0.12\ M_\odot$ yr^{-1}. Consequently, Σ_{SFR} for regions in the LIRGs ranges from 7–402 $M_\odot$ yr^{-1} kpc^{-2} with a median of $197 \pm 78\ M_\odot$ yr^{-1} kpc^{-2}, about an order of magnitude higher than for regions in the normal galaxies, whose Σ_{SFR} ranges from 0.4–9.2 $M_\odot$ yr^{-1} kpc^{-2} with a median of $1.4 \pm 0.9\ M_\odot$ yr^{-1} kpc^{-2}. We discuss the potential effect of resolution on the results in Section 6.3.

5.4. Thermal Fractions at 33 GHz

Radio continuum captures both nonthermal synchrotron emission of cosmic-ray electrons accelerated by supernovae and thermal free–free emission associated with H II regions of massive stars (<10 Myr). At high radio frequencies, radio emission has been directly related to ionizing photons produced by young massive stars (Murphy et al. 2012), with thermal fractions (i.e., ratio of thermal free–free emission to total radio continuum emission) $\gtrsim$90% at 33 GHz in individual star-forming regions in nearby spiral galaxies (Linden et al. 2020). However, it has been shown that even at 33 GHz, radio continuum emission in local U/LIRGs may be largely nonthermal, due to dust absorption of ionizing photons (Barcos-Muñoz et al. 2015, 2017).

To understand what is driving the 33 GHz radio continuum emission in our sample of nuclear rings on sub-kiloparsec scales, we estimate thermal fractions at 33 GHz, f_{th}, using the spectral index measured between 15 and 33 GHz (see Section 4.2) and

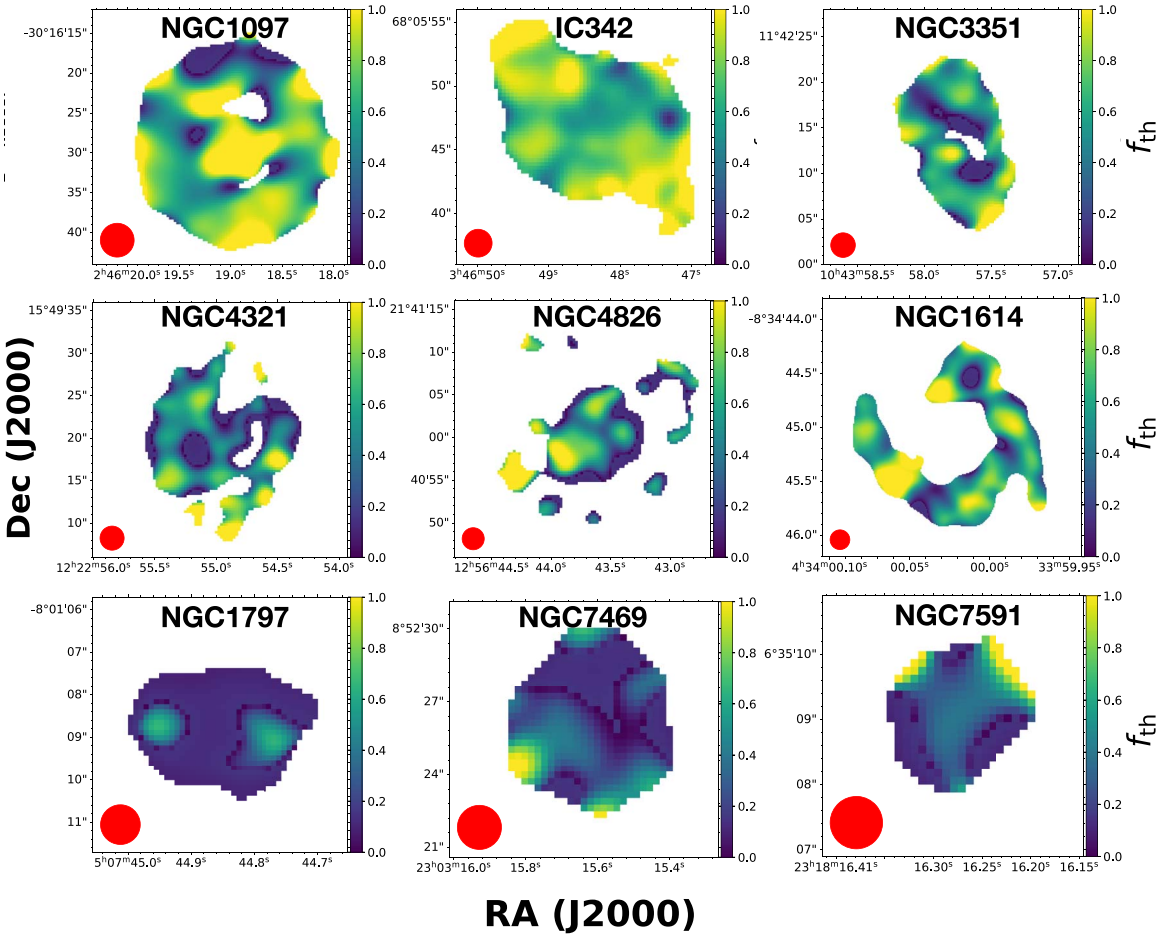

Figure 4. Maps of thermal fractions at 33 GHz of the sample galaxies. Each map was calculated from a pair of beam-matched 15 and 33 GHz images as described in Section 5.4. Red filled circles at the lower left of the maps represent the final matched beam. These maps show significant spatial variation in the distribution of thermal emission in these nuclear rings. Lower-resolution images are used for NGC 1797, NGC 7469, and NGC 7591.

Equation (11) from Murphy et al. (2012):

$$f_{\rm th}^{\nu_1} = \frac{(\nu_2/\nu_1)^{\alpha} - (\nu_2/\nu_1)^{\alpha_{\rm NT}}}{(\nu_2/\nu_1)^{-0.1} - (\nu_2/\nu_1)^{\alpha_{\rm NT}}} \quad (6)$$

where α is the spectral index measured between ν_1 and ν_2 (33 and 15 GHz), and $\alpha_{\rm NT}$ is the nonthermal spectral index. Almost all regions have $-0.85 < \alpha < -0.1$ within uncertainties, therefore we adopt $\alpha_{\rm NT} = -0.85$ for our calculations following Murphy et al. (2012). Out of the total of 58 NRSF regions, three have $\alpha \lesssim -0.85$, which means their radio continuum spectra between 15 and 33 GHz are steeper than the typical nonthermal spectrum. In these cases we set $\alpha_{\rm NT} = \alpha - 0.1$ based on previous measurements of the maximum dispersion of nonthermal spectral index given by $\sigma_{\alpha_{\rm NT}} \simeq 0.1$ (Niklas et al. 1997; Murphy et al. 2011, 2012). Additionally, three NRSF regions have $\alpha \gtrsim -0.1$, in which cases we set $f_{\rm th}$ to 100%, assuming the spectral flattening is caused by increasing thermal fraction. Alternatively, it may have originated from $\alpha_{\rm NT}$ flattening or anomalous microwave emission (e.g., Dickinson et al. 2018), which will require future matched-resolution observations at more than two radio frequencies to confirm.

Here we use only 15 and 33 GHz images to estimate $f_{\rm th}$ because 3 GHz observations from the GOALS equatorial survey do not resolve the ring structures except in NGC 7469. Linden et al. (2020) observed similar spectral steepness at 3–33 GHz and 15–33 GHz for the full SFRS sample, therefore we do not expect to overestimate 33 GHz thermal fractions in NRSF regions in the normal galaxies by using only 15 and 33 GHz measurements. However, in a study of extranuclear SF regions in local LIRGs, Linden et al. (2019) observed a steeper spectral profile at 3–33 GHz than at 15–33 GHz on kiloparsec scales. Therefore the thermal fractions estimated at 33 GHz for the sample of NRSF regions in LIRGs may be higher than reported here when matched-resolution observations at 3 GHz are included, despite the fact that we did not observe significant spectral flattening at 15–33 GHz compared to 3–33 GHz in NGC 7469.

To better visualize the free–free emission distribution in these rings, we additionally construct pixel-by-pixel maps of $f_{\rm th}$, as shown in Figure 4. We mask all values below $5\sigma_{\rm rms}$ for 15 and 33 GHz beam-matched images to ensure reliable outputs, after which we calculate α and $f_{\rm th}$ at each pixel. These maps show significant spatial variation in the distribution of thermal emission in these nuclear rings, with areas of high $f_{\rm th}$ mostly corresponding to the identified NRSF regions. Variations in $f_{\rm th}$ on scales smaller than the matched beams are highly correlated and therefore not physically significant.

The estimated $f_{\rm th}$ has ranges of 35%–100% and 4%–100% for NRSF regions in the normal galaxies and in the LIRGs, respectively. We note that low-resolution ($\sim$0.″6 or 200 pc) 15 and 33 GHz images were used to calculate $f_{\rm th}$ for NGC 1797, NGC 7469, and NGC 7591 because the high-resolution images

do not have strong enough detection for robust measurements. This means that the physical scales at which $f_{\rm th}$ is measured are 2–5 times larger than the spatial extent of the identified regions, likely including areas with little SF or diffuse nonthermal emission (i.e., cosmic rays accelerated by supernovae). This can skew $f_{\rm th}$ toward lower values, and therefore values reported in Table 6 may be interpreted as lower limits. We further discuss the implications of these results in Section 6.5.

5.5. Gas Depletion Times

In the left panels of Figure 5, we show the beam-matched CO ($J = 1$–0) moment 0 maps (in color) and 33 GHz continuum data (in contour) for the six nuclear rings in the sample that have archival CO ($J = 1$–0) data at resolutions comparable to the VLA data (Section 3.2). We can see that the nuclear rings observed in the radio continuum are largely co-spatial with the cold molecular gas, and molecular spiral arms are visible beyond the rings in NGC 1097, IC 342, NGC 3351, and NGC 4321. Using the measurements of CO ($J = 1$–0) and 33 GHz continuum emission on these resolution-matched maps, we can calculate the cold molecular gas mass ($M_{\rm mol}$) and surface densities ($\Sigma_{\rm mol}$) in these six nuclear rings and their individual NRSF regions, and make direct comparisons with the SFR and $\Sigma_{\rm SFR}$ to estimate the timescale on which SF depletes the molecular gas, which is used in both observational and theoretical studies to quantify star formation efficiencies (i.e., $\tau_{\rm dep} = 1/{\rm SFE} = \Sigma_{\rm mol}/\Sigma_{\rm SFR}$; e.g., Bigiel et al. 2008; Wilson et al. 2019; Moreno et al. 2021).

We follow Herrero-Illana et al. (2019) and use an equation from Solomon et al. (1992) to convert the measured CO ($J = 1$–0) flux to molecular gas mass:

$$M_{\rm mol} = \alpha_{\rm CO} L'_{\rm CO} \tag{7}$$

$$= 2.45 \times 10^3 \alpha_{\rm CO} \left(\frac{S_{\rm CO}\Delta\nu}{\rm Jy\ km\ s^{-1}}\right)\left(\frac{D_L}{\rm Mpc}\right)^2 (1+z)^{-1} \tag{8}$$

where $M_{\rm mol}$ is in units of $M_\odot$, $S_{\rm CO}\Delta\nu$ is the integrated line flux in Jy km s^{-1} and D_L is the luminosity distance in Mpc reported in Table 1 given the redshift z. Finally, $\alpha_{\rm CO}$ is the CO-to-H_2 conversion factor, in units of $M_\odot$ (K km s^{-1} pc^{-2})$^{-1}$. We adopt $\alpha_{\rm CO} = 4.3\,M_\odot$ (K km s^{-1} pc^{-2})$^{-1}$ for the five nuclear rings hosted in normal galaxies following previous resolved studies of nearby disk galaxies (Bigiel et al. 2008; Leroy et al. 2013), and we use the U/LIRG value $\alpha_{\rm CO} = 1.8\,M_\odot$ (K km s^{-1} pc^{-2})$^{-1}$ from Herrero-Illana et al. (2019) for the nuclear ring in NGC 7469. We use Equation (1) to convert the 33 GHz continuum flux to SFR, and $\Sigma_{\rm SFR}$ and $\Sigma_{\rm mol}$ are calculated using the physical areas of the adopted apertures (see Section 4.3). In Table 7 we summarize the derived quantities for the nuclear rings and the individual NRSF regions.

Based on calculations using previous global CO ($J = 1$–0) measurements (Young et al. 1996; Crosthwaite 2001; Crosthwaite et al. 2001; García-Burillo et al. 2003; Davies et al. 2004), these six nuclear rings contain ∼10%–30% of the total molecular gas mass of their host galaxies; this gas is available to fuel the active starbursts that are responsible for ∼10%–60% of the total SFR of the host galaxies. The average $\Sigma_{\rm mol}$ ranges from 280 ± 40 to $900 \pm 90\,M_\odot$ yr^{-1} pc^{-2} in these nuclear rings, and from 84 ± 180 to $1970 \pm 200\,M_\odot$ yr^{-1} pc^{-2} in the NRSF regions. The gas depletion times $\tau_{\rm dep}$ associated with the individual NRSF regions range from 0.07 to 1.4 Gyr. The median $\tau_{\rm dep}$ for regions in the normal galaxies is 0.6 ± 0.5 Gyr. This is almost an order of magnitude longer than for regions in NGC 7469, which has a median $\tau_{\rm dep}$ of 0.08 ± 0.01 Gyr. These values agree with results from previous sub-kiloparsec studies of normal galaxies (Bigiel et al. 2008; Leroy et al. 2013) and U/LIRGs (Wilson et al. 2019). Although our measurements are made on scales larger than the region sizes measured using native resolution radio maps, the median $\tau_{\rm dep}$ for the NRSF regions is largely consistent with $\tau_{\rm dep}$ measured over the entire ring for each galaxy, therefore higher-resolution measurements may increase the scatter of $\tau_{\rm dep}$ estimated for these regions but will not significantly change the results. In the right panels of Figure 5, we also show a pixel-by-pixel map of $\tau_{\rm dep}$ for each nuclear ring for more direct visualization. We note that $\tau_{\rm dep}$ derived near AGNs is not meaningful because the 33 GHz emission is not associated solely with star formation, and hence we also do not report $\Sigma_{\rm SFR}$ and $\tau_{\rm dep}$ in Table 7 for regions containing an AGN. We further discuss these results in the context of a universal star formation relation (e.g., Kennicutt 1998) in Section 6.6.

6. Discussion

Our selection criterion has resulted in the identification of NRSF in four LIRGs and five normal galaxies. The NRSF in our sample exhibits diverse spatial distributions (Figures 1(a) and (b)). For example, NGC 1097 and NGC 1614 have more randomly distributed NRSF regions along the rings than NGC 3351 and NGC 1797, where bright regions occur on opposite sides of the ring. Several studies have discussed the potential mechanisms that may give rise to certain alignments of bright NRSF regions, such as orbit crowding of gas clouds at the ends of nuclear stellar bars (e.g., Kenney & Lord 1991; Mazzarella et al. 1994; Englmaier & Shlosman 2004), or specific gas inflow rates into the ring (e.g., Seo & Kim 2013). Depending on how gas accumulates, NRSF can take place either stochastically in the ring due to gravitational instability, resulting in a random spatial distribution of "hotspots", or close to the contact points between the ring and dust lanes in multiple bursts (e.g., Böker et al. 2008). Given the limited sample size, we do not further discuss the implications associated with the NRSF spatial distribution, but simply provide descriptions of our observations and relevant information from previous studies on individual nuclear rings in Appendix A. Instead, we focus our discussions on the implications of the results in Section 5, and the limitations of the present sample.

6.1. Sample Limitation

The sample presented in this work is limited by several effects. Given the resolution of the observations, a nuclear ring has to have an angular radius larger than the synthesized beam in order for the ring structure to be resolved. An example is NGC 4579, a known nuclear ring host in SFRS, whose ring radius is estimated to be 1.″6 from Hubble Space Telescope (HST) optical and near-IR observations (Comerón et al. 2010), which is smaller than the 33 GHz beam size of ∼2″, and it is therefore not included in our sample. Additionally, the surface brightness of the nuclear ring must be high enough above the sensitivity limits of the observations for the ring structure to be visually distinct. NGC 4736 and NGC 5194 are two other galaxies from SFRS that are included in Comerón et al. (2010)

Table 6
Region Properties

Galaxy	ν (GHz)	ID	S_ν (mJy)	R_e (pc)	SFR ($M_\odot$ yr^{-1})	$\Sigma_{\rm SFR}$ ($M_\odot$ yr^{-1} kpc^{-2})	α	$f_{\rm th}$ (%)	Nucleus
(1)	(2)	(3)	(4)	(5)	(6)	(7)	(8)	(9)	(10)
NGC 1097	33	1	0.92 ± 0.12	142 ± 22	0.10 ± 0.01	1.5 ± 0.1	-0.18 ± 0.23	91 ± 24	
	33	2	0.85 ± 0.16	117 ± 25	0.09 ± 0.02	2.0 ± 0.1	-0.25 ± 0.22	84 ± 24	
	33	3	2.00 ± 0.25	184 ± 27	0.21 ± 0.03	1.9 ± 0.1	-0.44 ± 0.20	62 ± 26	
	33	4	1.09 ± 0.08	123 ± 12	0.11 ± 0.01	2.4 ± 0.1	-0.50 ± 0.21	54 ± 28	
	33	5	3.48 ± 0.04	163 ± 6	N/A	N/A	-0.02 ± 0.19	100 ± 17	AGN
	33	6	0.64 ± 0.11	113 ± 21	0.07 ± 0.01	1.6 ± 0.1	-0.52 ± 0.23	51 ± 32	
	33	7	0.89 ± 0.60	121 ± 85	0.09 ± 0.06	2.0 ± 0.5	-0.32 ± 0.23	77 ± 27	
	33	8	0.42 ± 0.07	104 ± 18	0.04 ± 0.01	1.3 ± 0.1	-0.05 ± 0.30	100 ± 28	
	33	9	1.40 ± 0.08	164 ± 14	0.15 ± 0.01	1.7 ± 0.1	-0.40 ± 0.21	66 ± 26	
IC 342	33	1	12.3 ± 0.42	49 ± 3	0.07 ± 0.01	9.2 ± 0.2	-0.33 ± 0.18	75 ± 21	
	33	2	0.86 ± 0.12	16 ± 3	0.01 ± 0.01	5.9 ± 0.3	-0.36 ± 0.19	72 ± 23	
	33	3	2.10 ± 0.25	23 ± 3	0.01 ± 0.01	6.8 ± 0.3	-0.27 ± 0.18	82 ± 20	
	33	4	0.86 ± 0.12	17 ± 3	0.01 ± 0.01	5.4 ± 0.3	-0.20 ± 0.19	90 ± 20	
NGC 3351	33	1	1.50 ± 0.07	167 ± 15	0.07 ± 0.01	0.78 ± 0.02	-0.44 ± 0.19	62 ± 24	
	33	2	0.19 ± 0.04	58 ± 13	0.01 ± 0.01	0.82 ± 0.06	-0.62 ± 0.22	37 ± 33	
	33	3	1.20 ± 0.05	118 ± 8	0.05 ± 0.01	1.2 ± 0.1	-0.43 ± 0.18	62 ± 24	
NGC 4321	33	1	0.06 ± 0.01	<72	0.01 ± 0.01	>0.42	-0.30 ± 0.35	79 ± 40	
	33	2	0.33 ± 0.03	119 ± 15	0.04 ± 0.01	0.79 ± 0.04	-0.35 ± 0.21	73 ± 25	
	33	3	0.20 ± 0.04	110 ± 26	N/A	N/A	-0.63 ± 0.24	35 ± 36	AGN
	33	4	0.17 ± 0.03	85 ± 17	0.02 ± 0.01	0.80 ± 0.06	-0.52 ± 0.22	51 ± 31	
	33	5	0.09 ± 0.03	77 ± 25	0.01 ± 0.01	0.51 ± 0.06	-0.61 ± 0.29	38 ± 42	
	33	6	0.11 ± 0.03	68 ± 19	0.01 ± 0.01	0.78 ± 0.07	-0.47 ± 0.23	57 ± 31	
NGC 4826	33	1	0.47 ± 0.05	44 ± 6	N/A	N/A	-0.47 ± 0.19	58 ± 26	AGN
	33	2	0.44 ± 0.03	40 ± 4	0.01 ± 0.01	1.3 ± 0.1	-0.51 ± 0.19	53 ± 26	
	33	3	0.34 ± 0.03	38 ± 4	0.01 ± 0.01	1.1 ± 0.1	-0.30 ± 0.21	78 ± 24	
NGC 1614	33	1	0.27 ± 0.03	27 ± 4	0.65 ± 0.07	275 ± 47	-0.55 ± 0.31	47 ± 44	
	33	2	0.06 ± 0.01	15 ± 3	0.14 ± 0.03	213 ± 68	-0.38 ± 0.39	68 ± 48	
	33	3	0.05 ± 0.04	14 ± 9	0.13 ± 0.08	208 ± 193	-0.31 ± 0.38	77 ± 44	
	33	4	0.04 ± 0.01	<14	0.10 ± 0.03	>149	-0.79 ± 0.36	10 ± 60	
	33	5	0.08 ± 0.02	18 ± 5	0.20 ± 0.06	204 ± 83	-0.28 ± 0.44	81 ± 50	
	33	6	0.17 ± 0.19	22 ± 26	0.41 ± 0.45	266 ± 433	-0.07 ± 0.30	100 ± 29	
	33	7	0.08 ± 0.02	16 ± 5	0.19 ± 0.06	241 ± 110	-0.33 ± 0.34	76 ± 39	
	33	8	0.08 ± 0.02	16 ± 4	0.19 ± 0.04	249 ± 88	-0.43 ± 0.32	63 ± 40	
	33	9	0.03 ± 0.02	<14	0.08 ± 0.03	>136	-0.74 ± 0.34	18 ± 55	
	33	10	0.10 ± 0.06	16 ± 10	0.25 ± 0.15	306 ± 277	-0.39 ± 0.33	67 ± 41	
	33	11	0.04 ± 0.01	<14	0.09 ± 0.03	>135	-0.85 ± 0.57	15 ± 86	Starburst
	33	12	0.06 ± 0.01	<14	0.15 ± 0.03	>241	-0.46 ± 0.29	59 ± 38	
	33	13	0.20 ± 0.03	22 ± 4	0.48 ± 0.08	311 ± 82	-0.27 ± 0.30	82 ± 33	
	33	14	0.15 ± 0.03	18 ± 6	0.36 ± 0.07	327 ± 94	-0.36 ± 0.28	71 ± 34	
	33	15	0.45 ± 0.07	31 ± 4	1.1 ± 0.16	366 ± 85	-0.26 ± 0.25	83 ± 27	
	33	16	0.12 ± 0.02	19 ± 3	0.28 ± 0.05	236 ± 66	-0.45 ± 0.40	60 ± 52	
	33	17	0.04 ± 0.01	13 ± 4	0.10 ± 0.03	197 ± 83	-0.03 ± 0.43	100 ± 40	
	33	18	0.07 ± 0.02	17 ± 6	0.17 ± 0.06	207 ± 103	-0.36 ± 0.33	71 ± 40	
	33	19	0.10 ± 0.03	14 ± 4	0.25 ± 0.06	402 ± 150	-0.89 ± 0.24	15 ± 34	
	33	20	0.09 ± 0.02	<14	0.21 ± 0.04	>326	-0.80 ± 0.24	8 ± 41	
	33	21	0.16 ± 0.03	19 ± 4	0.38 ± 0.07	316 ± 92	-0.55 ± 0.27	47 ± 38	
NGC 1797	33	1	0.18 ± 0.02	<100	0.38 ± 0.05	>12	-0.78 ± 0.21	11 ± 35	
	33	2	0.68 ± 0.03	194 ± 12	1.4 ± 0.05	12 ± 1	-0.67 ± 0.19	28 ± 30	
	33	3	0.35 ± 0.04	126 ± 17	0.73 ± 0.08	14 ± 3	-0.68 ± 0.20	28 ± 32	
	33	4	0.11 ± 0.02	<99	0.23 ± 0.04	>7.4	-1.19 ± 0.22	12 ± 26	
NGC 7469	33	1	0.64 ± 0.11	221 ± 45	1.7 ± 0.29	11 ± 3	-0.57 ± 0.18	43 ± 27	
	33	2	0.60 ± 0.07	157 ± 24	1.6 ± 0.19	20 ± 4	-0.79 ± 0.18	10 ± 31	
	33	3	6.06 ± 0.20	268 ± 30	N/A	N/A	-0.74 ± 0.18	19 ± 29	AGN
	33	4	0.17 ± 0.04	90 ± 23	0.45 ± 0.11	18 ± 6	-0.83 ± 0.18	4 ± 32	
	33	5	0.24 ± 0.04	96 ± 20	0.61 ± 0.11	21 ± 6	-0.74 ± 0.18	17 ± 30	
	33	6	0.19 ± 0.03	<95	0.49 ± 0.07	>17	-0.88 ± 0.18	15 ± 27	
NGC 7591	15	1	0.14 ± 0.03	21 ± 5	0.27 ± 0.07	197 ± 69	-0.64 ± 0.18	34 ± 27	
	15	2	0.12 ± 0.04	21 ± 7	0.22 ± 0.07	165 ± 77	-0.66 ± 0.18	30 ± 28	
	15	3	0.12 ± 0.02	19 ± 5	0.22 ± 0.05	197 ± 63	-0.63 ± 0.18	35 ± 27	
	15	4	0.09 ± 0.02	19 ± 5	0.17 ± 0.04	139 ± 46	-0.65 ± 0.18	32 ± 28	

Table 6
(Continued)

Galaxy	ν (GHz)	ID	S_ν (mJy)	R_e (pc)	SFR ($M_\odot$ yr^{-1})	$\Sigma_{\rm SFR}$ ($M_\odot$ yr^{-1} kpc^{-2})	α	$f_{\rm th}$ (%)	Nucleus
(1)	(2)	(3)	(4)	(5)	(6)	(7)	(8)	(9)	(10)
	15	5	0.05 ± 0.01	18 ± 5	N/A	N/A	-0.63 ± 0.18	35 ± 27	AGN
	15	6	0.11 ± 0.02	22 ± 6	0.21 ± 0.04	130 ± 43	-0.63 ± 0.18	35 ± 27	
	15	7	0.40 ± 0.24	46 ± 30	0.76 ± 0.47	115 ± 103	-0.64 ± 0.18	34 ± 28	

Note. (1) Host galaxy of the nuclear ring. (2) Frequency at which regions were identified and SFR and sizes were measured. For NGC 7591, the 15 GHz image was used instead. (3) Identifier of the region in reference to Figure 3. (4) Flux density of the region. (5) Effective radius of the region assuming it is circular (Section 5.3). Beam areas are used for unresolved regions as upper limits for their sizes, indicated by "<". (6) SFR calculated using Equations (1) and (5) for non-AGN regions. (7) $\Sigma_{\rm SFR}$ estimated by dividing (6) by region area $A = \pi R_e^2$ (in kpc^2). Unresolved regions are given lower limits for their $\Sigma_{\rm SFR}$, indicated by ">". (8) Spectral index associated with the region (Section 5.4) measured from 15 to 33 GHz. (9) Fraction of thermal emission at 33 GHz estimated using α (Section 4.2). Given the coarser resolution of the beam-matched 15 and 33 GHz images on which α was measured, the reported 33 GHz thermal fractions may be considered as lower limits. See Section 6.5 for discussion. (10) Whether the region corresponds to a galactic nucleus (AGN/starburst); see Table 1 for references.

but excluded from our sample because many of their NRSF regions are too faint for the ring structure to be visually distinct. This may be due to the overall lower level of SF activity, and/or a lack of sensitivity of the observations. For example, with an estimated angular radius of 50″ (1.2 kpc, Comerón et al. 2010), the ring in NGC 4736 is detected close to the edge of the 33 GHz primary beam, where sensitivity is significantly worse than in the phase center, which results in incomplete detection of the ring structure.

For observations from the GOALS equatorial survey, rings at very close distances, such as the one in NGC 1068, become too highly resolved at A configuration to be detected given the sensitivity limit, and rings that are far away may either have been unresolved or lack consistent detection of NSRF regions for the ring structure to be visually identified. The fact that all four LIRGs in our sample have similar luminosity distances at ~70 Mpc may be the result of such a trade-off between physical resolution and sensitivity. Finally, rings that are highly inclined may appear linear and therefore are not represented in our sample. High-resolution kinematics studies are needed to reveal these edge-on rings.

Given the above, our sample represents a lower limit to the number of nuclear rings in both surveys, and thus the results derived in this study may not represent the full range of NRSF properties in SFRS and the GOALS equatorial survey.

6.2. The Majority of SF in These LIRGs Takes Place in Their Nuclear Rings

Figure 6 shows the fraction of total SFR contributed by the nuclear ring with respect to $L_{\rm IR}$ of the host galaxy, as calculated in Section 5.2. Each galaxy is color-coded by its $L_{\rm IR}$, with darker blue and darker red representing lower and higher $L_{\rm IR}$, respectively. Nuclear rings hosted in the LIRGs have up to six times higher $\rm SFR_{ring}/SFR_{tot}$ than those hosted in the normal galaxies. Furthermore, we can also see that high $\rm SFR_{ring}/SFR_{tot}$ in general corresponds to galaxies with high $L_{\rm IR}$. This result echoes previous studies, which found that local galaxies with higher $L_{\rm IR}$ have more centrally concentrated emission (Díaz-Santos et al. 2010, 2011) and that the nuclear SF in LIRGs can dominate the properties of their host galaxies (e.g., Veilleux et al. 1995; Soifer et al. 2001). However, the nuclear rings we study here may represent only the most extreme cases, and it is possible that in many LIRGs the total star formation is less centrally concentrated. We will present results on various nuclear SF structures in the entire GOALS equatorial survey in a forthcoming paper to further investigate this.

It is also worth noting that NGC 1097, which is interacting with a dwarf companion, has both the highest $L_{\rm IR}$ and the highest $\rm SFR_{ring}/SFR_{tot}$ among the normal galaxies. This trend is consistent with studies that observed excess nuclear SFR in interacting galaxies relative to isolated systems (e.g., Lonsdale et al. 1984; Bushouse 1986), which is also predicted in simulations of galaxy interaction (Moreno et al. 2021).

6.3. High SFR and Σ_{SFR} in NRSF Regions in the Sample of LIRGs

The consistently higher nuclear ring contribution to the total SFR, as discussed in the last section, points to more active NRSF in our sample of LIRGs. In Figure 7, we show, as filled symbols, the SFR and $\Sigma_{\rm SFR}$ of all 58 NRSF regions with respect to their effective radius R_e (reported in Table 6), and as open symbols, the integrated values for the entire rings (Table 4). Note that for the integrated values, $R_e = \sqrt{\rm area/\pi}$ measures the effective extent of the ring, and is different from $R_{\rm peak}$ defined in Section 4.1.

Despite the different angular resolutions of the observations, the physical resolutions achieved (marked by short vertical lines on the horizontal axis) and the effective sizes of NRSF regions measured are similar between the normal galaxies and the LIRGs. We can see that at similar or smaller effective sizes, the integrated rings and NRSF regions in the LIRGs (triangles) both have at least an order of magnitude higher SFR and $\Sigma_{\rm SFR}$ than their counterparts in the normal galaxies (squares), confirming that NRSF in these LIRGs is indeed more active than in the normal galaxies. Additionally, most NRSF regions in these LIRGs have SFR as high as the integrated ring values of the normal galaxies, with 1–2 dex smaller effective sizes, exhibiting an extremely high spatial concentration of SF activities.

It is worth noting that for both the normal galaxies and the LIRGs, regions measured at the highest physical resolutions (i.e., those in IC 342 and NGC 1614) have the highest $\Sigma_{\rm SFR}$, which demonstrates the importance of high-resolution observations in accurate characterization of these regions. Lower-resolution observations would likely result in diluted (and thus lower) measures of the intrinsic $\Sigma_{\rm SFR}$. Assuming the extreme case where $\Sigma_{\rm SFR}$ is diluted by quiescent regions with no active SF when measured within a larger area (i.e., $\Sigma_{\rm SFR} \propto 1/R_e^2$,

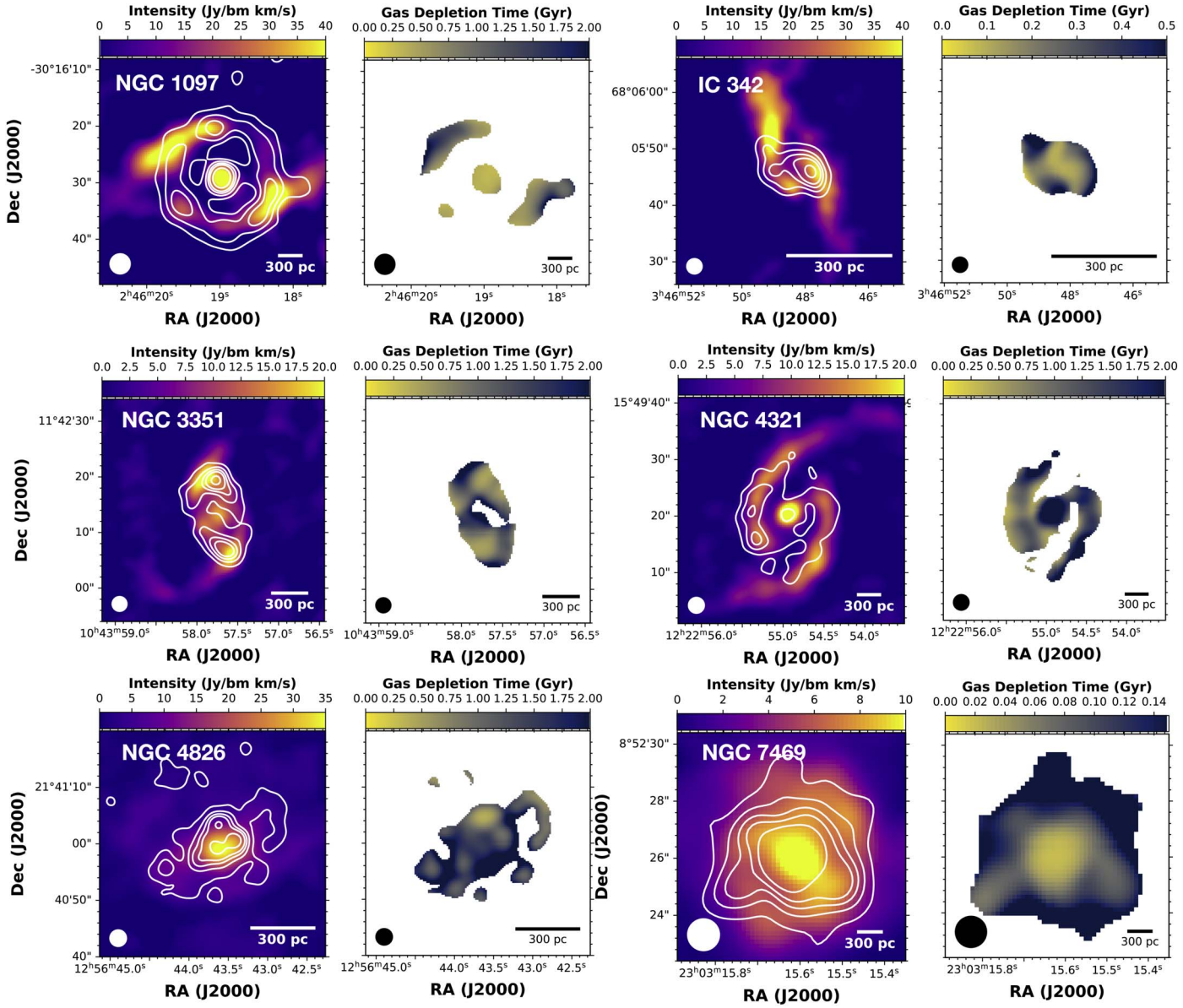

Figure 5. Six nuclear rings with high-resolution archival CO ($J = 1$–0) data sets. For each galaxy panel, left: beam-matched archival CO ($J = 1$–0) moment 0 map (in color) and VLA 33 GHz continuum image (white contour). The contours corresponds to levels of 5, 10, 15, 20, 30 $\sigma_{\rm rms}$ in 33 GHz intensity; right: maps of gas depletion time $\tau_{\rm dep} = \Sigma_{\rm mol}/\Sigma_{\rm SFR}$, using maps shown on the left. Matched beams are represented by white/black filled circles on the lower left of each image in the left/right panel. The radio continuum is largely co-spatial with cold molecular gas. In NGC 1097, IC 342, NGC 3351, and NGC 4321, prominent spiral structures overlap with the SF nuclear rings and extend farther out into the galactic disks. The spiral structure in NGC 7469 is much more tightly wound and less distinct, and its nuclear ring has gas depletion times that on average are an order of magnitude shorter.

hatched in red in Figure 7), NRSF regions in NGC 1614 may appear to have similar $\Sigma_{\rm SFR}$ to resolved regions in the normal galaxies even at 0.″3 resolution (100 pc). The fact that regions in NGC 1797 and NGC 7469 share similar $\Sigma_{\rm SFR}$ with regions in IC 342 is likely a result of such a dilution effect, given that observations of these two galaxies have much lower physical resolutions.

Furthermore, many regions in the LIRGs, especially in NGC 1614, are unresolved by the beam (marked with arrows), which means that their sizes can be even smaller, and their $\Sigma_{\rm SFR}$ can be even higher. Additionally, the integrated ring values for these LIRGs all lie above the ranges spanned by their NRSF regions, suggesting that active SF takes place throughout these nuclear rings, not only in the NRSF regions that we characterized here. Indeed, the sum of SFR in the NRSF regions only accounts for about 20%–50% of the total SFR of the rings. If higher-resolution deep observations were to be made available for these rings, we would expect to detect more NRSF regions that are less luminous or much smaller.

In summary, the NRSF regions studied in our sample of LIRGs intrinsically have higher SFR and $\Sigma_{\rm SFR}$ with sizes similar to or smaller than their counterparts in the sample of normal galaxies. Observations with consistent, high physical resolution are crucial for accurate characterization of these extreme, compact NRSF regions.

We note that within our sample, we do not find evidence associating AGN activity with NRSF, because SFR or $\Sigma_{\rm SFR}$ in NRSF regions does not appear consistently higher or lower in AGN hosts. Existing measurements of AGN strength indicators in the IR and X-ray of the host galaxies (Stierwalt et al. 2013;

Table 7
Quantities Derived from Resolution-matched 33 GHz and CO ($J = 1$–0) Maps

	Galaxy	ID	A_{ap} (arcsec^2)	M_{mol} ($10^6\,M_\odot$)	Σ_{mol} ($M_\odot$ yr^{-1} pc^{-2})	Σ_{SFR} ($M_\odot$ yr^{-1} kpc^{-2})	τ_{dep} (Gyr)
	(1)	(2)	(3)	(4)	(5)	(6)	(7)
Ring	NGC 1097	⋯	577	760 ± 100	280 ± 40	0.72 ± 0.07	0.38 ± 0.06
	IC 342	⋯	213	47 ± 5	860 ± 90	2.9 ± 0.3	0.29 ± 0.04
	NGC 3351	⋯	170	190 ± 20	550 ± 60	0.55 ± 0.05	1.0 ± 0.1
	NGC 4321	⋯	312	430 ± 40	280 ± 30	0.26 ± 0.03	1.1 ± 0.2
	NGC 4826	⋯	82	50 ± 5	790 ± 80	0.58 ± 0.06	1.4 ± 0.2
	NGC 7469	⋯	25	2500 ± 1	890 ± 90	8.8 ± 0.9	0.10 ± 0.01
Region	NGC 1097	1	13.4	26 ± 10	410 ± 20	1.2 ± 0.1	0.35 ± 0.14
		2	10.14	47 ± 10	970 ± 200	1.6 ± 0.2	0.61 ± 0.15
		3	22.5	49 ± 14	450 ± 130	1.5 ± 0.2	0.32 ± 0.09
		4	10.1	61 ± 11	1260 ± 220	1.5 ± 0.2	0.82 ± 0.17
		5	17.6	90 ± 15	1070 ± 170	N/A	N/A
		6	10.1	35 ± 10	730 ± 190	1.2 ± 0.1	0.63 ± 0.18
		7	10.1	14 ± 9	290 ± 180	1.3 ± 0.1	0.23 ± 0.15
		8	10.1	4.1 ± 8.7	84 ± 180	0.68 ± 0.10	0.12 ± 0.27
		9	18.0	63 ± 13	740 ± 150	1.3 ± 0.1	0.58 ± 0.14
	IC 342	1	29.4	11 ± 3	1460 ± 150	7.7 ± 0.8	0.19 ± 0.03
		2	5.93	2.5 ± 1.1	1610 ± 160	4.6 ± 0.5	0.35 ± 0.05
		3	6.80	1.7 ± 1.2	990 ± 100	5.1 ± 0.6	0.19 ± 0.03
		4	5.93	3.0 ± 1.1	1970 ± 200	4.0 ± 0.5	0.49 ± 0.08
	NGC 3351	1	43.0	54 ± 6	620 ± 70	0.66 ± 0.07	0.94 ± 0.14
		2	5.72	7.8 ± 1.1	680 ± 100	0.71 ± 0.08	0.95 ± 0.17
		3	21.4	34 ± 4	780 ± 90	1.0 ± 0.1	0.75 ± 0.11
	NGC 4321	1	6.31	20 ± 2	660 ± 80	0.29 ± 0.05	2.30 ± 0.46
		2	9.26	26 ± 3	580 ± 70	0.61 ± 0.07	0.94 ± 0.15
		3	7.86	49 ± 5	1270 ± 130	N/A	N/A
		4	6.31	14 ± 2	440 ± 60	0.62 ± 0.07	0.70 ± 0.13
		5	6.31	16 ± 2	530 ± 70	0.38 ± 0.05	1.4 ± 0.3
		6	6.31	18 ± 2	590 ± 70	0.57 ± 0.07	1.0 ± 0.2
	NGC 4826	1	9.39	9.2 ± 0.9	1450 ± 150	N/A	N/A
		2	7.58	5.8 ± 0.6	1140 ± 120	1.0 ± 0.1	1.1 ± 0.2
		3	6.94	1.9 ± 0.3	420 ± 60	0.74 ± 0.07	0.57 ± 0.09
	NGC 7469	1	1.40	280 ± 30	750 ± 100	8.5 ± 0.9	0.09 ± 0.01
		2	0.98	290 ± 30	1130 ± 130	12 ± 1	0.09 ± 0.01
		3	2.04	800 ± 80	1480 ± 150	N/A	N/A
		1	0.98	290 ± 30	1110 ± 130	17 ± 2	0.07 ± 0.01
		2	0.98	270 ± 30	1060 ± 120	12 ± 1	0.08 ± 0.01
		3	0.98	280 ± 30	1090 ± 130	13 ± 1	0.09 ± 0.01

Note. (1) Host galaxy of the nuclear ring. (2) Identifier of the region in reference to Figure 3. (3) Area of the circular aperture used to measure 33 GHz and CO ($J = 1$–0) flux of the nuclear ring/NRSF region. For IC 342 and NGC 4826, beam areas are subtracted from the ring areas defined by R_{out} to account for the central unresolved cavities. (4) Molecular gas mass derived from CO ($J = 1$–0) flux measurements (see Section 5.5). (5) Molecular gas surface density over the physical areas of the adopted apertures. (6) Star formation rate surface density over the physical areas of the adopted apertures for non-AGN regions. (7) Gas depletion time calculated using (5) and (6) for non-AGN regions.

Dale et al. 2006; Grier et al. 2011) also do not reveal any correlation with the NRSF properties studied here.

6.4. NRSF in These LIRGs Has SFR and Σ_{SFR} Comparable to Luminous SF Regions at High z

Using high-resolution HST Paα and Paβ observations, Larson et al. (2020) measured the SFR and effective radii of 751 extranuclear SF regions and 59 nuclei in 48 local LIRGs from GOALS. The authors showed that SF in local LIRGs bridges the gap between the local universe and the high-z universe, with a wide range of SFR overlapping with that found in luminous SF clumps in $z = 1$–4 lensed galaxies. In Figure 8, we reproduce Figures 4 and 5 from Larson et al. (2020), overlaid with radio measurements for the individual NRSF regions from this study. Note that the most luminous regions in Larson et al. (2020) are the nuclei, most of which have SFR $> 0.1\,M_\odot$ yr^{-1} and $\Sigma_{SFR} > 0.2\,M_\odot$ yr^{-1} kpc^{-2} with effective radii greater than 300 pc. The dashed vertical line in orange marks the resolution limit of 90 pc for measurements from Larson et al. (2020). There are several conclusions that can be drawn from this figure.

1. For the five normal galaxies from SFRS, the NRSF regions (black squares) have higher SFR and Σ_{SFR} than the ensemble of SINGS regions (gray dots), which are measured in the disks of normal galaxies. Similarly, for the sample of LIRGs from the GOALS equatorial survey, the NRSF regions (red triangles) have higher SFR and Σ_{SFR} than the ensemble of GOALS regions (orange "+") detected in the near IR, over 90% of which are extranuclear. These two results together suggest that NRSF can be more extreme than extranuclear SF in the disk of the host galaxy, supporting findings from Linden et al. (2019).

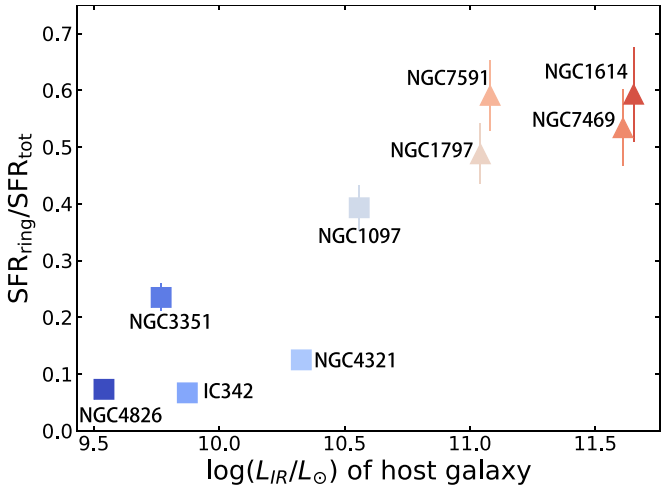

Figure 6. Fraction of total SFR contributed by the nuclear ring with respect to L_{IR} of the host galaxy. See Section 4.1 and Tables 4 and 5 for details. Each galaxy is color-coded by its L_{IR}, with darker blue and darker red representing lower and higher L_{IR}, respectively. Squares and triangles represent normal galaxies and LIRGs, respectively. Nuclear rings in the LIRGs consistently contribute to higher fractions of the total SFR of their host galaxies than rings in the normal galaxies.

2. At similar measured sizes, NRSF regions in the sample of normal galaxies overlap with the extranuclear GOALS regions in Larson et al. (2020) and lower-luminosity lensed regions at high z (purple "×"). On the other hand, NRSF regions in the sample of LIRGs lie above the extranuclear GOALS regions from Larson et al. (2020), and their SFR and Σ_{SFR} are comparable to those of many luminous high-z regions. Note that if we consider the same dilution analysis as shown in Figure 7 (in red hatching), we would still find that the NRSF regions in the LIRGs have Σ_{SFR} comparable to many high-z SF regions with lower-resolution measurements. We will investigate whether this applies more broadly to other nuclear SF regions in the GOALS equatorial survey in the upcoming paper. Future surveys with the capability of detecting fainter and smaller NRSF regions will allow a more comprehensive understanding of NRSF in LIRGs.

We also note that the different SFR tracers used for data presented in Figure 8 are sensitive to dust obscuration at different levels, which can affect the above interpretation of our results. While heavy nonuniform extinction in the nuclei of LIRGs can lead to underestimation of SFR and Σ_{SFR} by 1–1.5 dex even in the near IR (U et al. 2019), over 90% of the GOALS regions being compared here are extranuclear and expected to be mildly extincted (Larson et al. 2020). Therefore we do not expect extinction correction to change our conclusions.

6.5. Thermal Fractions in the NRSF Regions at 33 GHz

In Figure 9, we show the estimated thermal fractions at 33 GHz, f_{th}, associated with the NRSF regions in the sample nuclear rings with respect to the physical radii of the apertures within which these measurements were made (see Sections 4.2 and 5.4). For context, we also overlay the expected values from Barcos-Muñoz et al. (2017) for luminous nuclei in U/LIRGs (hatched red), and the median values from Linden et al. (2020)

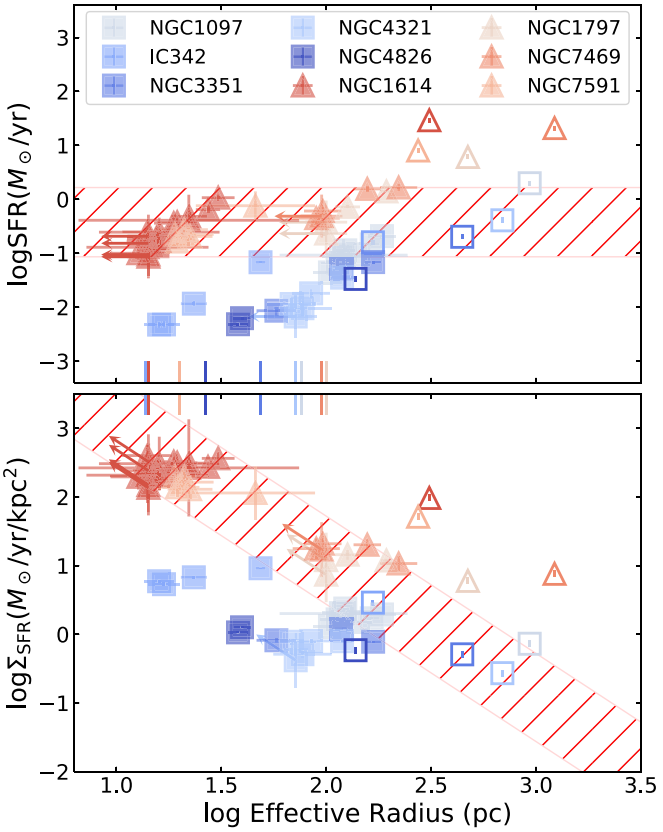

Figure 7. Effective radius R_e vs. SFR (top) and Σ_{SFR} (bottom). Values for the 58 NRSF regions are shown as filled symbols, and integrated ring values as open symbols, both color-coded by L_{IR} of the host galaxy, with squares and triangles representing normal galaxies and LIRGs, respectively. Arrows indicate upper limits to R_e for unresolved regions, which translate into lower limits to Σ_{SFR} given the measured SFR. Short vertical lines on the horizontal axis mark the resolution limits of the observations. The red hatching represents the range of SFR and expected range of Σ_{SFR} spanned by the smallest and largest NRSF regions in the sample of LIRGs, assuming the extreme case where Σ_{SFR} is diluted by quiescent areas when measured within a larger region size (i.e., $\Sigma_{SFR} \propto 1/R_e^2$). The NRSF regions studied in our sample of LIRGs have higher SFR and Σ_{SFR} with sizes similar to or smaller than their counterparts in the sample of normal galaxies.

for the nuclear regions in SFRS (hatched blue), both measured at sub-kiloparsec scales.

The median value of f_{th} associated with the NRSF regions in the sample of normal galaxies is $\sim$69% ± 19%, in agreement with the median value of $\sim$71% for all nuclear regions (i.e., having galactocentric radii $r_G < 250$ pc) in the full SFRS sample, reported in Linden et al. (2020). As discussed in Linden et al. (2020), excess nonthermal emission is present in the circumnuclear SF regions in SFRS compared to the extranuclear regions ($r_G \geqslant 1$ kpc; median $f_{th} \sim 90\%$), likely due to prolonged SF activities. As illustrated in Figure 6 of Linden et al. (2020) using Starburst99 models, continuous SF for over 100 Myr can decrease the thermal fraction to $\sim$50% due to accumulation of nonthermal emission from supernovae, while an instantaneous starburst can dramatically bring down the thermal fraction to much lower levels within 10 Myr. Given that nuclear rings have prolific episodic starbursts (e.g., Buta et al. 2000; Maoz et al. 2001) and can persist over gigayear timescales (Knapen et al. 1995; Seo & Kim 2013), the relatively low f_{th} observed in the NRSF regions in these normal galaxies may be driven by a combination of continuous and "bursty" SF.

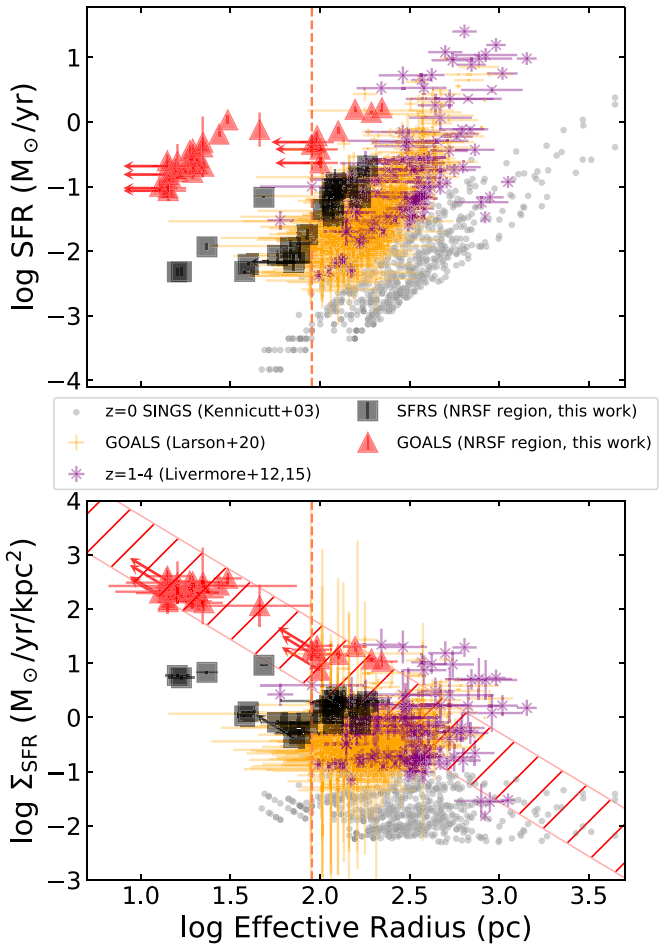

Figure 8. Effective radius R_e vs. SFR (top) and Σ_{SFR} (bottom) for SF regions in galaxies at different redshifts, reproduced from Figures 4 and 5 in Larson et al. (2020). Triangles and squares are radio continuum measurements of individual NRSF regions in the LIRGs from the GOALS equatorial survey (red) and the normal galaxies from SFRS (black). Arrows indicate lower limits to R_e and upper limits to Σ_{SFR} for unresolved regions. Purple "×" represent Hα measurements of SF regions in lensed galaxies at $z \simeq 1$–4 (Livermore et al. 2012, 2015). Orange "+" mark the Paα and Paβ measurements of 59 nuclei and 751 extranuclear SF regions in 48 local LIRGs from GOALS (Larson et al. 2020), with a resolution limit of 90 pc (orange dashed vertical line). Grey dots are Hα measurements of SF regions in SINGS galaxies. NRSF regions in the sample of local LIRGs have SFR and Σ_{SFR} comparable to or higher than luminous SF regions at high z.

In Figure 9 we also see that at similar physical scales, f_{th} can be even lower for NRSF regions in the sample of LIRGs than for those in the normal galaxies, except for NGC 1614, whose NRSF regions span a wide range in f_{th}. The median f_{th} in the NRSF regions in the sample of LIRGs is $\sim$35% $\pm$ 36% including NGC 1614, and $\sim$29% $\pm$ 9% excluding NGC 1614, which are much lower than the median of 69% measured in the normal galaxies. This is in agreement with findings from Barcos-Muñoz et al. (2015, 2017) that the nuclear regions in U/LIRGs are mostly dominated by nonthermal emission. These authors suggest that thermal emission in the nuclei of U/LIRGs may be suppressed via the absorption of ionizing photons by dust. However, in our case, the lower f_{th} can also be explained by beam dilution due to low resolutions of the beam-matched images, i.e., measurements for most regions in NGC 1797, NGC 7469, and NGC 7591 are at scales 2–5 times larger than the sizes of the NRSF regions characterized using Astrodendro. The wide range of f_{th} observed in the nuclear ring of NGC 1614, which is measured at physical scales smaller than 50 pc, has also been observed by Herrero-Illana et al. (2014). The authors conclude that this large variation reflects the different ages of starbursts in the NRSF regions, with regions of extremely young starbursts (<4 Myr) having thermal fractions $\sim$100%, and regions of old starbursts (>8 Myr) having much lower thermal fractions. This explanation is also consistent with Figure 6 in Linden et al. (2020). As demonstrated in previous sections, the NRSF regions in the sample of LIRGs are likely more compact than those in the normal galaxies. Therefore, measurements at 100–300 pc scales in these LIRGs may average over areas of young and old starbursts that have drastically different thermal content. Additionally, as mentioned in Section 5.4, nonthermal emission associated with supernovae can be more diffuse than thermal emission (e.g., Condon 1992), hence low-resolution measurements are more likely to represent nonthermal emission. It is possible that, at high resolutions (e.g., <100 pc), we may also see very high f_{th} in some of the NRSF regions in NGC 1797, NGC 7469, and NGC 7591, as observed in NGC 1614.

6.6. Star Formation Relation

Global measurements of Σ_{SFR} and Σ_{mol} of galaxies of various types indicate the existence of a universal SF relation, i.e., $\Sigma_{SFR} = A\Sigma_{mol}^N$, with $N \sim 1.4$ (e.g., Kennicutt 1998). According to this relation, SF efficiency increases (i.e., gas depletion time decreases) toward high Σ_{mol} for all types of galaxies. However, several studies argue for a bimodal SF relation that predicts constant star formation efficiency among galaxies of similar types, with gas depletion times in normal spiral galaxies 4–10 times longer than in U/LIRGs or high-z submillimeter galaxies (e.g., Bigiel et al. 2008; Daddi et al. 2010; Genzel et al. 2010; Kennicutt & de los Reyes 2021). As we show in Figure 10, this bimodality is also present in our results for the nuclear rings (open) and the NRSF regions (filled) derived from extinction-free measurements at sub-kiloparsec scales (see Section 5.5). Despite having 1–2 dex higher Σ_{mol}, the rings and the NRSF regions in the normal galaxies (square symbols) have similar gas depletion times ($\tau_{dep} \sim 1$ Gyr) to normal spiral disks. The ring and NRSF regions in NGC 7469 also show consistent τ_{dep} ($\sim$100 Myr), with circumnuclear disk measurements for U/LIRGs being up to an order of magnitude shorter than for rings and NRSF regions in the normal galaxies. This is similar to values measured in other sub-kiloparsec scale studies of U/LIRGs (e.g., Xu et al. 2015; Pereira-Santaella et al. 2016), but 4–6 times shorter than τ_{dep} estimated from global measurements of GOALS galaxies (Herrero-Illana et al. 2019). In a resolved study of five U/LIRGs, Wilson et al. (2019) demonstrated that τ_{dep} decreases more rapidly with increasing Σ_{mol} for $\Sigma_{mol} > 10^3\ M_\odot\ pc^{-2}$ in these extreme systems. In an upcoming paper, we will present sub-kiloparsec measurements for a larger sample of nuclear SF regions in the GOALS equatorial survey to further explore the sub-kiloparsec SF relation in local U/LIRGs.

The nuclear rings in IC 342 and NGC 1097 also have relatively high SFE compared to spiral disks and other nuclear rings hosted in normal galaxies, with $\tau_{dep} \sim 0.4$ Gyr. This central enhancement of SFE has also been observed in other studies of IC 342 (Sage & Solomon 1991; Pan et al. 2014) and in surveys of normal galaxies (e.g., Leroy et al. 2013; Utomo et al. 2017). Meanwhile, at similar Σ_{SFR}, NRSF regions in NGC 1097 span $\sim$1 dex in τ_{dep}. Tabatabaei et al. (2018) discovered that this large scatter in SFE is closely tied to local buildup of the magnetic fields that support molecular clouds against gravitational collapse. Overall, our results show that, in these nuclear rings, at similar Σ_{mol}, τ_{dep} is shorter in the LIRG NGC 7469 than in the normal galaxies, but it varies

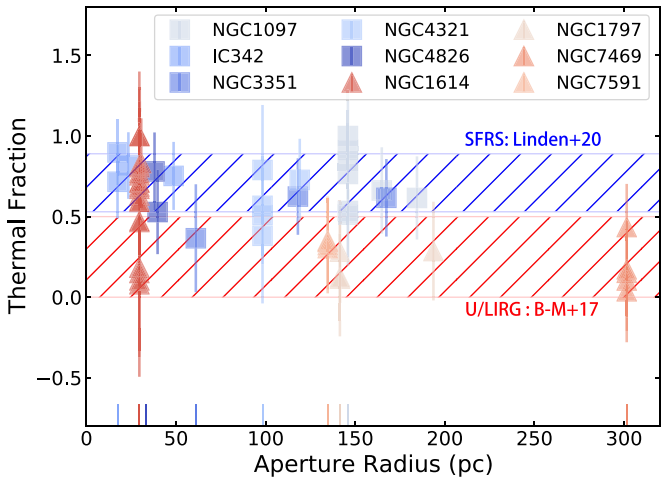

Figure 9. Thermal fraction at 33 GHz with respect to the physical size of the aperture used for the measurements for the NRSF regions. Each region is color-coded by L_{IR} of its host galaxy, and squares and triangles represent normal galaxies and LIRGs separately. Short vertical lines on the horizontal axis indicate resolution limits of the spectral index measurements (see Section 5.3). The blue hatched area marks the median values and median absolute deviation of 71% and ±18% measured by Linden et al. (2020) on 100–500 pc scales for the nuclear regions ($r_G < 250$ pc) in the SFRS sample, and the red hatched area represents the values for the nuclei in the most luminous local U/LIRGs (≲50%) predicted by Barcos-Muñoz et al. (2017) at similar physical scales. When measured at similar physical scales, NRSF regions in the sample of LIRGs seem to have lower thermal fractions than regions in the sample of normal galaxies. NRSF regions in NGC 1614, which are measured at the smallest physical scales, span a wide range in thermal fraction.

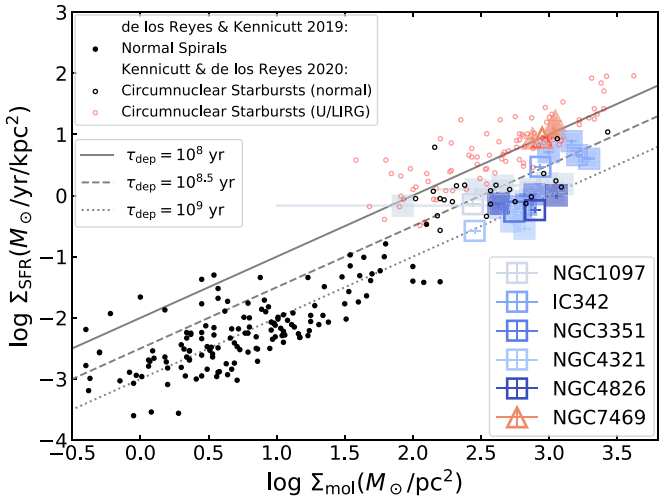

Figure 10. Σ_{mol} vs. Σ_{SFR} for the integrated nuclear rings (open) and NRSF regions (filled), color-coded by L_{IR} of the host galaxy. Also shown are global measurements for the normal spiral galaxies (black filled circles) from de los Reyes et al. (2019) and for circumnuclear starbursts in normal galaxies (black open circles) and U/LIRGs (red open circles) from Kennicutt & de los Reyes (2021), converted to match with the α_{CO} we adopted. Solid, dashed, and dotted gray lines represent gas depletion times τ_{dep} of 10^8, $10^{8.5}$, and 10^9 yr. The estimated τ_{dep} is shortest in the nuclear ring of NGC 7469, and has a large scatter among nuclear rings in the normal galaxies at similar Σ_{mol}.

among the normal galaxies as well, likely reflecting variation in local SF conditions. Tentatively, this supports the idea of a multimodal star formation relation on sub-kiloparsec scales. We note that adopting a normal galaxy α_{CO} for NGC 7469, or environmentally dependent α_{CO} (Narayanan et al. 2012; Sandstrom et al. 2013), can potentially produce a more continuous SF relation among these nuclear rings, but more statistics are needed to explore this.

7. Summary

In this paper we present analyses of VLA radio continuum observations at sub-kiloparsec resolution of nine nuclear rings hosted in four local LIRGs from the GOALS equatorial survey (NGC 1614, NGC 1797, NGC 7469, and NGC 7591) and five nearby normal galaxies from the SFRS (NGC 1097, IC 342, NGC 3351, NGC 4321, and NGC 4826). These two surveys map the brightest 3, 15, and 33 GHz radio continuum emission in 56 nearby normal galaxies and 68 local U/LIRGs at matched physical resolution, and hence allow direct, extinction-free comparison of nuclear star formation across different host environments. Using high-resolution maps of 33 or 15 GHz continuum, we characterize the size, SFR, and Σ_{SFR} of these nine detected nuclear rings and 57 individual NRSF regions at ∼100 pc scales. We summarize our main findings as follows.

1. The five nuclear rings in normal galaxies contribute 7%–40% of the total SFR of their host galaxies, with radii, SFR, and Σ_{SFR} in the ranges 43–599 pc, 0.03–2.0 $M_\odot$ yr^{-1}, and 0.27–2.90 $M_\odot$ yr^{-1} kpc^{-2}, respectively. By comparison, the four nuclear rings in the LIRGs have much more dominant contributions to the total star formation of their host galaxies, at 49%–60%, with radii, SFR, and Σ_{SFR} in the ranges 121–531 pc, 6.1–29 $M_\odot$ yr^{-1}, and 6.0–97 $M_\odot$ yr^{-1} kpc^{-2}, respectively.
2. We identified a total of 57 individual NRSF regions using Astrodendro, 22 of which are hosted in the five normal galaxies and 35 in the LIRGs. NRSF regions in the normal galaxies have effective radii, SFR, and Σ_{SFR} in the ranges 16–184 pc, 0.01–0.21 $M_\odot$ yr^{-1}, and 0.4–9.2 $M_\odot$ yr^{-1} kpc^{-2}, respectively. NRSF regions in the LIRGs have similar ranges of effective radii, of 13–221 pc, but their SFR and Σ_{SFR} are an order of magnitude higher, with ranges of 0.08–1.7 $M_\odot$ yr^{-1} and 7–402 $M_\odot$ yr^{-1} kpc^{-2}, respectively. Many of these NRSF regions in the LIRGs are unresolved by our observations, so they may be more compact with higher intrinsic Σ_{SFR}. We also found that these NRSF regions in the LIRGs have SFR and Σ_{SFR} as extreme as measured in lensed high-z SF galaxies from the literature.
3. The median ratio of thermal emission to the total 33 GHz radio continuum emission (i.e., thermal fraction) associated with the NRSF regions is 69% ± 19% in the normal

galaxies, and 35% ± 36% in the LIRGs, which is lower than estimates for extranuclear SF regions but consistent with results from previous studies. The dominant presence of nonthermal emission in the LIRGs may originate from suppression of thermal emission due to absorption of ionizing photons by highly concentrated dust in H II regions. In our case, it is more likely due to insufficient resolution of the measurements that results in the inclusion of more diffuse nonthermal emission from cosmic rays accelerated by supernovae. A wide range of thermal fractions were observed in NGC 1614 at high resolution (<100 pc), which likely reflects different ages of the starbursts along the nuclear ring.

4. For all five normal galaxies and one LIRG (NGC 7469), we use available archival CO ($J = 1$–0) data with comparable resolutions to our 33 GHz observations to further study star formation efficiencies in these nuclear rings at sub-kiloparsec scales. The nuclear rings and NRSF regions in the normal galaxies have gas depletion times $\tau_{\rm dep} \sim 1$ Gyr, about an order of magnitude longer than in the nuclear ring and NRSF regions of NGC 7469 ($\tau_{\rm dep} \sim 100$ Myr), which is consistent with results from previous studies on kiloparsec and global scales. However, $\tau_{\rm dep}$ estimated for rings and regions with similar $\Sigma_{\rm mol}$ has a fair amount of scatter, which may point to a multimodal star formation relation on sub-kiloparsec scales. More statistics are needed to explore this.

In this work we have demonstrated the ability to study embedded nuclear ring star-forming regions on sub-kiloparsec scales in local LIRGs using high-frequency radio continuum as an extinction-free tracer of star formation. This makes it possible to directly compare the properties of star formation in the heavily obscured hearts of local U/LIRGs with those at the center of normal galaxies. We also show that to fully resolve and characterize these extremely compact NRSF regions in the local LIRGs, observations at even higher resolutions and better sensitivity are needed. Future facilities such as the ngVLA will greatly improve our understanding of deeply embedded compact nuclear structures in these systems.

We thank the anonymous reviewer for providing detailed and constructive feedback that significantly improved this manuscript. We also thank M. de los Reyes for sharing data points from Kennicutt & de los Reyes (2021), and V. Casasola and S. Ishizuki for making their data for NGC 4826 and IC 342 available online. Y.S. thanks the staff at National Radio Astronomy Observatory for providing valuable guidance on ALMA data reduction, and Alejandro Saravia, Eduardo Rodas-Quito, and William Meynardie for helpful discussions. A.S.E. and Y.S. were supported by NSF grant AST 1816838. Y.S. and S.T.L. acknowledge support by the NRAO Grote Reber Dissertation Fellowship. The National Radio Astronomy Observatory is a facility of the National Science Foundation operated under cooperative agreement by Associated Universities Inc. A.S.E. was also supported by the Taiwan, ROC, Ministry of Science and Technology grant MoST 102-2119-M-001-MY3. H.I. acknowledges support from JSPS KAKENHI Grant No. JP21H01129. V.U acknowledges support from the NASA Astrophysics Data Analysis Program (ADAP) grant 80NSSC20K0450. This research has made use of the NASA/IPAC Extragalactic Database (NED), which is funded by the National Aeronautics and Space Administration and operated by the California Institute of Technology. This research has also made use of NASA's Astrophysics Data System.

This paper makes use of the following ALMA data:

ADS/JAO.ALMA#2012.1.00001.S,
ADS/JAO.ALMA#2013.1.00885.S,
ADS/JAO.ALMA#2015.1.00978.S,
ADS/JAO.ALMA#2016.1.00972.S,
ADS/JAO.ALMA#2013.1.00218.S.

ALMA is a partnership of ESO (representing its member states), NSF (USA) and NINS (Japan), together with NRC (Canada), MOST and ASIAA (Taiwan), and KASI (Republic of Korea), in cooperation with the Republic of Chile. The Joint ALMA Observatory is operated by ESO, AUI/NRAO, and NAOJ.

Facilities: VLA(NRAO), ALMA(NRAO), NASA/IPAC Extragalactic Database (NED), NASA's Astrophysics Data System.

Software: Ned Wright's Cosmology Calculator (Wright 2006), Astropy (Astropy Collaboration et al. 2013; Price-Whelan et al. 2018), Astrodendro (http://www.dendrograms.org/), CASA (McMullin et al. 2007).

Appendix A
Notes on Individual Galaxies

Here we provide description of individual sources based on data used in this work, as displayed in Figures 1(a), (b), 2, and 5. Where relevant, we include descriptions from prior studies of each nuclear ring.

NGC 1097. In all three VLA bands, we clearly see a nearly circular star-forming ring with diameter $D \sim 17''$ (1.2 kpc) made of multiple bright SF knots surrounding a luminous nucleus. Emissions from the nucleus and the ring are well separated in the azimuthally averaged light profile at 33 GHz, which allows us to characterize the spatial extent of the ring. A nuclear spiral inside the ring, which is transporting gas into the nucleus through the ring, has been revealed with multi-wavelength observations by Prieto et al. (2019). Our radio images also show three faint streamer-like structures that connect the central nucleus to the ring, with the brightest streamer on the west of the nucleus extending a few arcseconds beyond the ring. This extension has a bright counterpart in the ALMA CO ($J = 1$–0) data, which coincides with the contact point of a kiloparsec gas streamer feeding into the ring, as discovered by Prieto et al. (2019). The host galaxy ($cz = 1270$ km s^{-1}) is interacting with at least one dwarf companion (1097A: $cz = 1368$ km s^{-1}) (Bowen et al. 2016).

IC 342. A small asymmetric nuclear star-forming ring ($D \sim 6''$, 160 pc) made of at least four distinct SF knots is detected at all three VLA bands. At 33 GHz, diffuse emission from the ring covers the central region, as seen in the azimuthally averaged light profile. No bright nuclear emission is detected at any VLA band, and the ring morphology has previously been confirmed in near-IR and CO observations (Boker et al. 1997; Schinnerer et al. 2003). Therefore we do not assign an inner radius for this nuclear ring when calculating its SFR to account for the diffuse emission, but the area of the synthesized beam is subtracted from the area defined by the outer radius when estimating $\Sigma_{\rm SFR}$ to account for the central cavity. In a previous molecular gas study, Ishizuki et al. (1990) suggest that the nuclear ring outlines the ends of a pair of molecular ridges, which may have been formed by shock waves from a bar-like gravitational potential.

NGC 3351. An elliptical nuclear ring ($D \sim 13''$, 600 pc) with an inclination angle of $\sim 59°$ is clearly present in images at all three VLA bands, with two bright SF knots lying on the north and south tips of the ring separately, accompanied by smaller, fainter SF knots on the east and west sides. The azimuthally averaged light profile at 33 GHz reveals a faint nuclear component, which outlines the inner radius of the ring. This component is most visible at 3 GHz. A comparison of the radio-detected ring with archival Spitzer IRAC 3.6 μm image of the galaxy reveals a bar-like stellar structure connecting the brightest radio "hotspots" along the north–south direction. Low-resolution ($\sim 7''$) molecular observations have suggested the presence of a molecular nuclear bar (Devereux et al. 1992), which is absent from the ALMA CO ($J = 1$–0) observation.

NGC 4321. The nuclear ring ($D \sim 14''$, 1 kpc) was detected at all three bands, along with the central LINER nucleus. The ring appears fairly clumpy, with three bright knots making up the east half of the ring and relatively faint diffuse emission on the west half. At 3 GHz more diffuse emission is detected, and the ring reveals itself to be part of a tightly wound spiral structure, which is also evident in the ALMA CO ($J = 1$–0) data. The ends of the molecular spiral arms correspond to the location of bright SF knots, which connect the ring to a nuclear bar that is prominent in both an archival Spitzer IRAC 3.6 μm image and CO data (Sakamoto et al. 1995). Numerical simulations predict that such nuclear bars exert strong gravitational torques on molecular gas to effectively feed the supermassive black holes and nuclear/circumnuclear starbursts (Wada et al. 1998).

NGC 4826. The small nuclear ring ($D \sim 5''$, 120 pc) is most apparent at 15 GHz, where we see five distinct knots lying close together to form a nearly circular structure. The brightest knot is the off-center LINER nucleus (García-Burillo et al. 2003). At 33 and 3 GHz, the emission from the two fainter knots is blended into the brighter knot in between them. The bright nuclear ring is also closely surrounded by a series of much fainter SF regions, which show up in the azimuthally averaged light profile at $\sim 10''$ (250 pc) away from the center (we exclude them from our analyses). At 33 GHz, diffuse emission from the ring covers the central region, as seen in the light profile. No bright nuclear emission is detected at any VLA band, and the ring morphology has previously been confirmed in CO observation (García-Burillo et al. 2003). Therefore we do not assign an inner radius for this nuclear ring when calculating its SFR to account for the diffuse emission, but the area of the synthesized beam is subtracted from the area defined by $R_{\rm out}$ when estimating $\Sigma_{\rm SFR}$ to account for the central cavity.

NGC 1614. A clumpy, almost circular nuclear star-forming ring ($D \sim 1.5''$, 400 pc), made of knots with various sizes and brightnesses, is detected at 33 and 15 GHz. One faint elongated knot to the west extends beyond the ring by $\sim 0\farcs5$ (150 pc). A faint nucleus surrounded by the ring is also detected at 33 GHz, which outlines the inner radius of the ring. At 3 GHz, the ring is unresolved. Prominant dust lanes have been observed to be connected to the northern tip of the nuclear ring, where molecular gas is potentially streaming into the ring and fueling the starbursts (Olsson et al. 2010; König et al. 2013).

NGC 1797. The ring structure is resolved for the very first time with the GOALS equatorial survey. At 33 GHz, we clearly see three bright SF knots connected by diffuse emission, forming an elliptical ring ($D \sim 2''$, 800 pc) with an inclination angle of $\sim 45°$. At 15 GHz, the brightest region on the east half of the ring is further resolved into three smaller distinct SF knots, with two brighter ones on the north connected to each other. The ring morphology at 3 GHz follows that at 33 GHz, but the diffuse emission connecting the east and west halves of the ring becomes more prominent. No bright nuclear emission is detected at any VLA band, therefore we do not assign an inner radius for this nuclear ring when calculating its SFR to account for the diffuse emission, but the area of the synthesized beam is subtracted from the area defined by $R_{\rm out}$ when estimating $\Sigma_{\rm SFR}$ to account for the central cavity.

NGC 7469. The ring structure ($D \sim 3''$, 1000 pc) containing five SF knots is clearly detected at 33 GHz, surrounding a much brighter Seyfert 1 nucleus, which outlines the inner radius of the ring. The ring appears more spiral-like at 3 GHz, where the northern and southern components are much more pronounced and extend beyond the ring. A similar morphology is also seen in ALMA CO ($J = 1$–0) data. Due to low angular resolution, the ring appears as faint diffuse emission surrounding the bright nucleus at 15 GHz. Mazzarella et al. (1994) observed the nuclear ring in the near IR, and found that the brightest SF "hotspots" coincide with the ends of a nuclear stellar bar revealed in K-band continuum, which may be transporting gas from the ring to the luminous Seyfert 1 nucleus (e.g., Wada et al. 1998).

NGC 7591. The elliptical ring ($D \sim 1''$, 300 pc) has an inclination angle of $\sim 62°$, and is detected at all three bands but was only resolved with at least $3\sigma_{\rm rms}$ at 15 GHz, with the southern part of the ring brighter than the rest. At 3 and 33 GHz, the ring becomes completely unresolved. The nuclear ring has also been observed in the near-IR Paschen observations by Larson et al. (2020), but NRSF regions in the rings are resolved for the first time with the GOALS equatorial survey.

Appendix B
Integrated Measurements for Highly Elliptical Rings

For all but three galaxies (NGC 1797, NGC 3351, and NGC 7591), we measured the azimuthally averaged light profiles of each nuclear ring by computing the averaged brightness per pixel on a series of 1 pixel wide concentric circles overlaid on top of 33 GHz images, with their centers aligned with the central coordinates of the host galaxy, with minor adjustments to visually match the ring center. Due to relatively high ellipticities of the nuclear rings in NGC 1797, NGC 3351, and NGC 7591, we used the following procedures to more accurately depict their light profiles. After each image is masked to preserve only emission with $\rm S/N > 5$, the coordinates of the unmasked pixels were extracted and then fitted with a 2D ellipse model using the least-squares fitting method suggested in Fitzgibbon et al. (1996). Note that the 15 GHz image was used for NGC 7591 instead due to low resolution of the available 33 GHz image. The model describes a generic quadratic curve:

$$ax^2 + 2bxy + cy^2 + 2dx + 2fy + g = 0 \qquad \text{(B1)}$$

where the fitted ellipse's center coordinate (x_0, y_0), semimajor and semiminor axes lengths (a', b'), and the counterclockwise angle of rotation from the x-axis to the major axis of the ellipse

could be calculated as follows:

$$x_0 = \frac{cd - bf}{b^2 - ac}$$

$$y_0 = \frac{af - bd}{b^2 - ac}$$

$$a' = \sqrt{\frac{2(af^2 + cd^2 + gb^2 - 2bdf - acg)}{(b^2 - ac)[\sqrt{(a-c)^2 + 4b^2} - (a + c)]}}$$

$$b' = \sqrt{\frac{2(af^2 + cd^2 + gb^2 - 2bdf - acg)}{(b^2 - ac)[-\sqrt{(a-c)^2 + 4b^2} - (a + c)]}}$$

$$\phi = \begin{cases} 0, & \text{for } b = 0 \text{ and } a < c \\ \frac{\pi}{2}, & \text{for } b = 0 \text{ and } a > c \\ \frac{1}{2}\cot^{-1}\left(\frac{a-c}{2b}\right), & \text{for } b \neq 0 \text{ and } a < c \\ \frac{\pi}{2} + \frac{1}{2}\cot^{-1}\left(\frac{a-c}{2b}\right), & \text{for } b \neq 0 \text{ and } a > c \end{cases}$$

The above method works under the condition that $\begin{vmatrix} a & b & d \\ b & c & f \\ d & f & g \end{vmatrix} \neq 0$, $\begin{vmatrix} a & b \\ b & c \end{vmatrix} > 0$, and $a + c < 0$, which makes Equation (B1) the general expression for 2D ellipses. The caveat is that this method does not work well for circular fits, therefore we adopt it only to extrapolate the properties of the highly elliptical rings in NGC 1797, NGC 3351, and NGC 7591. Based on the ellipticity estimated from the model fitting result, we then produced a series of concentric 1 pixel wide elliptical annuli to calculate the adjusted azimuthally averaged brightness of the ring.

ORCID iDs

Y. Song https://orcid.org/0000-0002-3139-3041
S. T. Linden https://orcid.org/0000-0002-1000-6081
A. S. Evans https://orcid.org/0000-0003-2638-1334
L. Barcos-Muñoz https://orcid.org/0000-0003-0057-8892
G. C. Privon https://orcid.org/0000-0003-3474-1125
I. Yoon https://orcid.org/0000-0001-9163-0064
E. J. Murphy https://orcid.org/0000-0001-7089-7325
K. L. Larson https://orcid.org/0000-0003-3917-6460
T. Díaz-Santos https://orcid.org/0000-0003-0699-6083
L. Armus https://orcid.org/0000-0003-3498-2973
Joseph M. Mazzarella https://orcid.org/0000-0002-8204-8619
J. Howell https://orcid.org/0000-0001-6028-8059
H. Inami https://orcid.org/0000-0003-4268-0393
N. Torres-Albà https://orcid.org/0000-0003-3638-8943
V. U https://orcid.org/0000-0002-1912-0024
V. Charmandaris https://orcid.org/0000-0002-2688-1956
J. McKinney https://orcid.org/0000-0002-6149-8178
D. Kunneriath https://orcid.org/0000-0002-1568-579X
E. Momjian https://orcid.org/0000-0003-3168-5922

References

Allard, E. L., Knapen, J. H., Peletier, R. F., & Sarzi, M. 2006, MNRAS, 371, 1087
Alonso-Herrero, A., Engelbracht, C. W., Rieke, M. J., Rieke, G. H., & Quillen, A. C. 2001, ApJ, 546, 952
Armus, L., Mazzarella, J. M., Evans, A. S., et al. 2009, PASP, 121, 559
Astropy Collaboration, Robitaille, T. P., Tollerud, E. J., et al. 2013, A&A, 558, A33
Athanassoula, E. 1994, in Mass-Transfer Induced Activity in Galaxies, ed. I. Shlosman (Cambridge: Cambridge Univ. Press), 143
Balzano, V. A. 1983, ApJ, 268, 602
Barcos-Muñoz, L., Leroy, A. K., Evans, A. S., et al. 2015, ApJ, 799, 10
Barcos-Muñoz, L., Leroy, A. K., Evans, A. S., et al. 2017, ApJ, 843, 117
Barreto, J. A., Downes, D., Combes, F., et al. 1991, A&A, 244, 257
Bigiel, F., Leroy, A., Walter, F., et al. 2008, AJ, 136, 2846
Böker, T., Falcón-Barroso, J., Schinnerer, E., Knapen, J. H., & Ryder, S. 2008, AJ, 135, 479
Boker, T., Forster-Schreiber, N. M., & Genzel, R. 1997, AJ, 114, 1883
Bowen, D. V., Chelouche, D., Jenkins, E. B., et al. 2016, ApJ, 826, 50
Brown, M. J. I., Moustakas, J., Smith, J. D. T., et al. 2014, ApJS, 212, 18
Bushouse, H. A. 1986, AJ, 91, 255
Buta, R., & Combes, F. 1996, Fund. Cosmic Phys., 17, 95
Buta, R., Treuthardt, P. M., Byrd, G. G., & Crocker, D. A. 2000, AJ, 120, 1289
Casasola, V., Hunt, L., Combes, F., & García-Burillo, S. 2015, A&A, 577, A135
Clark, C. J. R., Verstocken, S., Bianchi, S., et al. 2018, A&A, 609, A37
Combes, F. 2001, in Advanced Lectures on the Starburst-AGN, ed. I. Aretxaga, D. Kunth, & R. Mújica (Singapore: World Scientific), 223
Combes, F., & Gerin, M. 1985, A&A, 150, 327
Comerón, S., Knapen, J. H., Beckman, J. E., et al. 2010, MNRAS, 402, 2462
Condon, J. J. 1992, ARA&A, 30, 575
Crosthwaite, L. P. 2001, PhD Thesis, University of California, Los Angeles
Crosthwaite, L. P., Turner, J. L., Hurt, R. L., et al. 2001, AJ, 122, 797
Daddi, E., Elbaz, D., Walter, F., et al. 2010, ApJL, 714, L118
Dale, D. A., Smith, J. D. T., Armus, L., et al. 2006, ApJ, 646, 161
Dale, D. A., Smith, J. D. T., Schlawin, E. A., et al. 2009, ApJ, 693, 1821
Davies, R. I., Tacconi, L. J., & Genzel, R. 2004, ApJ, 602, 148
de los Reyes, M. A. C., Kennicutt, Robert C., J., & Robert, C. 2019, ApJ, 872, 16
Devereux, N. A., Kenney, J. D., & Young, J. S. 1992, AJ, 103, 784
Díaz-Santos, T., Armus, L., Charmandaris, V., et al. 2017, ApJ, 846, 32
Díaz-Santos, T., Charmandaris, V., Armus, L., et al. 2010, ApJ, 723, 993
Díaz-Santos, T., Charmandaris, V., Armus, L., et al. 2011, ApJ, 741, 32
Dickinson, C., Ali-Haïmoud, Y., Barr, A., et al. 2018, NewAR, 80, 1
Elbaz, D., Dickinson, M., Hwang, H. S., et al. 2011, A&A, 533, A119
Englmaier, P., & Shlosman, I. 2004, ApJL, 617, L115
Fitzgibbon, A. W., Pilu, M., & Fisher, R. B. 1996, in Proc. 13th Int. Conf. on Pattern Recognition (Piscataway, NJ: IEEE), 253
Fukuda, H., Wada, K., & Habe, A. 1998, MNRAS, 295, 463
García-Burillo, S., Combes, F., Hunt, L. K., et al. 2003, A&A, 407, 485
Genzel, R., Tacconi, L. J., Gracia-Carpio, J., et al. 2010, MNRAS, 407, 2091
Genzel, R., Weitzel, L., Tacconi-Garman, L. E., et al. 1995, ApJ, 444, 129
Grier, C. J., Mathur, S., Ghosh, H., & Ferrarese, L. 2011, ApJ, 731, 60
Haan, S., Armus, L., Surace, J. A., et al. 2013, MNRAS, 434, 1264
Herrero-Illana, R., Alberdi, A., Pérez-Torres, M. Á., et al. 2017, MNRAS, 470, L112
Herrero-Illana, R., Pérez-Torres, M. Á., Alonso-Herrero, A., et al. 2014, ApJ, 786, 156
Herrero-Illana, R., Privon, G. C., Evans, A. S., et al. 2019, A&A, 628, A71
Hinshaw, G., Weiland, J. L., Hill, R. S., et al. 2009, ApJS, 180, 225
Ho, L. C., Filippenko, A. V., & Sargent, W. L. W. 1997, ApJS, 112, 315
Hopkins, P. F., & Quataert, E. 2010, MNRAS, 407, 1529
Howell, J. H., Armus, L., Mazzarella, J. M., et al. 2010, ApJ, 715, 572
Hsieh, P.-Y., Matsushita, S., Liu, G., et al. 2011, ApJ, 736, 129
Ishizuki, S., Kawabe, R., Ishiguro, M., Okumura, S. K., & Morita, K.-I. 1990, Natur, 344, 224
Kenney, J. D. P., & Lord, S. D. 1991, ApJ, 381, 118
Kennicutt, R. C., Calzetti, D., Aniano, G., et al. 2011, PASP, 123, 1347
Kennicutt, Robert C., J. 1998, ApJ, 498, 541
Kennicutt, Robert C., J., Armus, L., Bendo, G., et al. 2003, PASP, 115, 928
Kennicutt, R. C., J., & de los Reyes, M. A. C. 2021, ApJ, 908, 61
Kim, W.-T., & Stone, J. M. 2012, ApJ, 751, 124
Knapen, J. H. 2005, A&A, 429, 141
Knapen, J. H., Beckman, J. E., Heller, C. H., Shlosman, I., & de Jong, R. S. 1995, ApJ, 454, 623
Knapen, J. H., Whyte, L. F., de Blok, W. J. G., & van der Hulst, J. M. 2004, A&A, 423, 481
König, S., Aalto, S., Muller, S., Beswick, R. J., & Gallagher, J. S. 2013, A&A, 553, A72
Kormendy, J., & Kennicutt, Robert C., J. 2004, ARA&A, 42, 603
Larson, K. L., Díaz-Santos, T., Armus, L., et al. 2020, ApJ, 888, 92
Laurikainen, E., & Salo, H. 2002, MNRAS, 337, 1118

Leaman, R., Fragkoudi, F., Querejeta, M., et al. 2019, MNRAS, 488, 3904
Leroy, A. K., Walter, F., Sandstrom, K., et al. 2013, AJ, 146, 19
Li, Z., Shen, J., & Kim, W.-T. 2015, ApJ, 806, 150
Linden, S. T., Murphy, E. J., Dong, D., et al. 2020, ApJS, 248, 25
Linden, S. T., Song, Y., Evans, A. S., et al. 2019, ApJ, 881, 70
Livermore, R. C., Jones, T., Richard, J., et al. 2012, MNRAS, 427, 688
Livermore, R. C., Jones, T. A., Richard, J., et al. 2015, MNRAS, 450, 1812
Lonsdale, C. J., Persson, S. E., & Matthews, K. 1984, ApJ, 287, 95
Ma, C., de Grijs, R., & Ho, L. C. 2018, ApJ, 857, 116
Maoz, D., Barth, A. J., Ho, L. C., Sternberg, A., & Filippenko, A. V. 2001, AJ, 121, 3048
Maoz, D., Barth, A. J., Sternberg, A., et al. 1996, AJ, 111, 2248
Mazzarella, J. M., Voit, G. M., Soifer, B. T., et al. 1994, AJ, 107, 1274
Mazzuca, L. M., Knapen, J. H., Veilleux, S., & Regan, M. W. 2008, ApJS, 174, 337
McMullin, J. P., Waters, B., Schiebel, D., Young, W., & Golap, K. 2007, in ASP Conf. Ser. 376, Astronomical Data Analysis Software and Systems XVI, ed. R. A. Shaw, F. Hill, & D. J. Bell (San Francisco, CA: ASP), 127
Moreno, J., Torrey, P., Ellison, S. L., et al. 2021, MNRAS, 503, 3113
Mould, J. R., Huchra, J. P., Freedman, W. L., et al. 2000, ApJ, 529, 786
Murphy, E. J., Bremseth, J., Mason, B. S., et al. 2012, ApJ, 761, 97
Murphy, E. J., Condon, J. J., Schinnerer, E., et al. 2011, ApJ, 737, 67
Murphy, E. J., Dong, D., Momjian, E., et al. 2018, ApJS, 234, 24
Narayanan, D., Krumholz, M. R., Ostriker, E. C., & Hernquist, L. 2012, MNRAS, 421, 3127
Niklas, S., Klein, U., & Wielebinski, R. 1997, A&A, 322, 19
Olsson, E., Aalto, S., Thomasson, M., & Beswick, R. 2010, A&A, 513, A11
Osterbrock, D. E., & Martel, A. 1993, ApJ, 414, 552
Pan, H.-A., Kuno, N., & Hirota, A. 2014, PASJ, 66, 27
Pereira-Santaella, M., Colina, L., García-Burillo, S., et al. 2016, A&A, 587, A44
Pereira-Santaella, M., Diamond-Stanic, A. M., Alonso-Herrero, A., & Rieke, G. H. 2010, ApJ, 725, 2270
Phillips, M. M., Pagel, B. E. J., Edmunds, M. G., & Diaz, A. 1984, MNRAS, 210, 701
Piqueras López, J., Colina, L., Arribas, S., & Alonso-Herrero, A. 2013, A&A, 553, A85
Planesas, P., Colina, L., & Perez-Olea, D. 1997, A&A, 325, 81
Price-Whelan, A. M., Sipőcz, B. M., Günther, H. M., et al. 2018, AJ, 156, 123
Prieto, M. A., Fernandez-Ontiveros, J. A., Bruzual, G., et al. 2019, MNRAS, 485, 3264
Regan, M. W., & Teuben, P. 2003, ApJ, 582, 723
Robitaille, T., Rice, T., Beaumont, C., et al. 2019, astrodendro: Astronomical data dendrogram creator, Astrophysics Source Code Library, ascl:1907.016
Sage, L. J., & Solomon, P. M. 1991, ApJ, 380, 392
Sakamoto, K., Okumura, S., Minezaki, T., Kobayashi, Y., & Wada, K. 1995, AJ, 110, 2075
Sanders, D. B., Mazzarella, J. M., Kim, D. C., Surace, J. A., & Soifer, B. T. 2003, AJ, 126, 1607
Sanders, D. B., & Mirabel, I. F. 1996, ARA&A, 34, 749
Sandstrom, K. M., Leroy, A. K., Walter, F., et al. 2013, ApJ, 777, 5
Sarzi, M., Allard, E. L., Knapen, J. H., & Mazzuca, L. M. 2007, MNRAS, 380, 949
Schinnerer, E., Böker, T., & Meier, D. S. 2003, ApJL, 591, L115
Seo, W.-Y., & Kim, W.-T. 2013, ApJ, 769, 100
Seo, W.-Y., & Kim, W.-T. 2014, ApJ, 792, 47
Shlosman, I., Begelman, M. C., & Frank, J. 1990, Natur, 345, 679
Soifer, B. T., Neugebauer, G., Matthews, K., et al. 2001, AJ, 122, 1213
Solomon, P. M., Downes, D., & Radford, S. J. E. 1992, ApJL, 398, L29
Speagle, J. S., Steinhardt, C. L., Capak, P. L., & Silverman, J. D. 2014, ApJS, 214, 15
Stierwalt, S., Armus, L., Surace, J. A., et al. 2013, ApJS, 206, 1
Storchi-Bergmann, T., Baldwin, J. A., & Wilson, A. S. 1993, ApJL, 410, L11
Tabatabaei, F. S., Minguez, P., Prieto, M. A., & Fernández-Ontiveros, J. A. 2018, NatAs, 2, 83
Telesco, C. M., & Decher, R. 1988, ApJ, 334, 573
U, V., Medling, A. M., Inami, H., et al. 2019, ApJ, 871, 166
U, V., Sanders, D. B., Mazzarella, J. M., et al. 2012, ApJS, 203, 9
Utomo, D., Bolatto, A. D., Wong, T., et al. 2017, ApJ, 849, 26
Veilleux, S., Kim, D. C., Sanders, D. B., Mazzarella, J. M., & Soifer, B. T. 1995, ApJS, 98, 171
Wada, K., Sakamoto, K., & Minezaki, T. 1998, ApJ, 494, 236
Wilson, C. D., Elmegreen, B. G., Bemis, A., & Brunetti, N. 2019, ApJ, 882, 5
Wright, E. L. 2006, PASP, 118, 1711
Xu, C. K., Cao, C., Lu, N., et al. 2015, ApJ, 799, 11
Young, J. S., Allen, L., Kenney, J. D. P., Lesser, A., & Rownd, B. 1996, AJ, 112, 1903
Zaragoza-Cardiel, J., Beckman, J., Font, J., et al. 2017, MNRAS, 465, 3461